HSV-1 exploits host heterochromatin for egress

Hannah C Lewis*[1,2], Laurel E Kelnhofer-Millevolte*[1,2,3], Mia R Brinkley[1], Hannah E Arbach[1], Edward A Arnold[1,4], Srinivas Ramachandran[5, 6, #], and Daphne C Avgousti[1,7,8, #]

1 Human Biology Division, Fred Hutchinson Cancer Research Center, 1100 Fairview Avenue North, Seattle, WA 98109

2 Molecular & Cellular Biology, Graduate Program, University of Washington and Fred Hutchinson Cancer Research Center, 1959 NE Pacific Street Box 357275 Seattle, WA 98195

3 UW Medical Scientist Training Program, 1959 NE Pacific Street Box 357470, Seattle, WA 98195

4 Microbiology Graduate Program, University of Washington, 1705 NE Pacific Street Box 357735, Seattle, WA 98195

5 RNA Bioscience Initiative, University of Colorado School of Medicine,

6 Department of Biochemistry and Molecular Genetics, University of Colorado School of Medicine, 12801 East 17th Avenue Mail Stop 8101, Aurora, CO 80045

7 Twitter: @avgousti_lab

8 Lead contact

* Authors contributed equally

Address correspondence to: srinivas.ramachandran@cuanschutz.edu (S.R.), avgousti@fredhutch.org (D.C.A.)

Abstract

Herpes simplex virus replicates and forms progeny in the nucleus where it must overcome host chromatin to establish a successful infection. During lytic infection, newly formed viral capsids navigate through heterochromatin channels at the nuclear periphery to egress out of the nucleus. In uninfected cells, specific histone modifications such as trimethylation on histone H3 lysine 27 (H3K27me3) and the histone variant macroH2A1 delineate heterochromatin regions, or repressed chromatin, that are predominantly located in the nuclear periphery. We examined these markers during HSV-1 lytic infection in primary cells and discovered a striking increase in the levels of macroH2A1 and H3K27me3. Here, we demonstrate that the loss of macroH2A1 results in significantly lower viral titers but does not impair viral transcription, protein production, or replication. By inhibiting the deposition of H3K27me3 by EZH2, we further show that reduction of H3K27me3 also leads to a significant decrease in viral titers. Through chromatin profiling of macroH2A1 and H3K27me3, we define the specific chromatin regions that change dynamically during HSV-1 lytic infection and show that regions with increased macroH2A1 and H3K27me3 correlate with decreased host transcription as measured by RNA-seq. Furthermore, we find by electron microscopy that loss of macroH2A1 results in reduced heterochromatin at the nuclear periphery and significantly more viral capsids trapped in the nuclear compartment. Using both high and low shedding clinical isolates of HSV-1, we similarly find that HSV-1 titers are significantly reduced in the absence of macroH2A1. Our work demonstrates that heterochromatin imposes an impediment for viral egress, but HSV-1 can exploit its dynamic nature to successfully mediate escape from the nucleus.

50 **INTRODUCTION**

51 Nuclear replicating viruses must contend with host chromatin to establish a successful infection.
52 Like most DNA viruses, herpes simplex virus (HSV-1) takes advantage of host histone factors
53 both by incorporating histones onto its genome to promote gene expression (*1*) and by
54 reorganizing host chromatin during infection (*2–4*). This redistribution of host chromatin results
55 in a global increase in heterochromatin (*5*), or transcriptionally repressed chromatin. Host
56 chromatin that is marginalized to the nuclear periphery during HSV-1 infection creates a
57 potential barrier for capsids to egress from the nucleus. Elegant electron microscopy work
58 showed that viral capsids traverse this dense chromatin in the nuclear periphery through
59 channels of less dense staining, termed heterochromatin channels (*6*). However, the
60 mechanisms by which these channels form are unclear.

61 In uninfected cells, specific histone modifications such as trimethylation of histone H3 lysine 27
62 (H3K27me3) and the histone variant macroH2A1 delineate heterochromatin regions that are
63 largely localized to the nuclear periphery. H3K27me3 is deposited by the EZH2 enzyme (*7*), a
64 member of the polycomb repressive complex (PRC2)(*8*). This modification is subsequently
65 bound by PRC2, leading to modification of adjacent nucleosomes, which results in formation of
66 dense heterochromatin and prevents transcription. The deposition of H3K27me3 is often
67 considered to be a consequence of slowed transcription and the regulation of PRC2 is intimately
68 linked to various biological processes including differentiation, proliferation, and maintaining cell
69 identity (*8*). H3K27me3 is heavily deposited on the inactive X chromosome in female mammals,
70 binding broad regions of the genome that overlap with macroH2A binding (*9*, *10*). MacroH2A,
71 the largest of the histone variants, consists of a canonical histone fold domain, a small linker
72 region and a C-terminal 25kDa macro domain that is thought to protrude from the nucleosome
73 (*11*). There are three isoforms referred to collectively as macroH2A: macroH2A1.1,
74 macroH2A1.2 and macroH2A2. MacroH2A1.1 and macroH2A1.2 are splice variants of the same
75 gene that differ by one exon resulting in a 28-amino acid difference in the macro domain. The
76 macro domain of macroH2A1.1 interacts directly with ADP-ribosylation, specifically through the
77 amino acids that differ from macroH2A1.2 (*12*, *13*). MacroH2A1 was also found to be
78 downregulated in melanoma (*14*), suggesting a key role in the maintenance of genome integrity.
79 Importantly, it was reported that loss of macroH2A1 and macroH2A2 results in a significant
80 decrease in heterochromatin in the nuclear periphery observed by electron microscopy (*15*).
81 Furthermore, macroH2A1 also demarcates regions of host chromatin that associate with the
82 nuclear lamina (*16*), termed lamina-associated domains (LADs). Given the complex role of

83 macroH2A in gene regulation and chromatin structure, studying its exploitation by a virus may
84 prove an important means to understanding its function.

85 Herpes simplex virus (HSV) infects an estimated two-thirds of the world's population where it
86 establishes latency and persists for the lifetime of the host (*17*, *18*). While most infections are
87 asymptomatic, HSV infection can have severe consequences in neonates and
88 immunocompromised individuals (*19–21*). During lytic infection, hundreds of host chromatin
89 factors are dynamically regulated (*3*). We hypothesized that several of these factors are
90 important for the formation of heterochromatin channels that allow HSV-1 to egress from the
91 nuclear compartment. We identified upregulation during HSV-1 infection of two key
92 heterochromatin markers: macroH2A1 and H3K27me3. Here, we use chromatin profiling via
93 Cleavage Under Targets and Tagmentation (CUT&Tag) of macroH2A1 and H3K27me3 to
94 define the specific host chromatin regions bound by these markers and how they change during
95 HSV-1 lytic infection. We show that regions with increased macroH2A1 and H3K27me3
96 correlate with decreased host transcription as measured by RNA-seq. Next, we demonstrate
97 that the loss of macroH2A1 results in significantly lower viral titers but does not impair viral
98 transcription, protein production, or replication. By inhibiting EZH2 deposition of H3K27me3, we
99 show that reduction of H3K27me3 also leads to a significant decrease in viral titers.
100 Furthermore, we demonstrate by transmission electron microscopy that loss of macroH2A1
101 results in reduced heterochromatin at the nuclear periphery and significantly more viral capsids
102 trapped in the nuclear compartment. Finally, we show that both high- and low-shedding clinical
103 isolates of HSV-1 also exhibit significantly reduced titers in the absence of macroH2A1. Our
104 study is the first to demonstrate that HSV-1 infection causes specific changes to
105 heterochromatin markers that are critical for efficient viral egress.

106

107 **RESULTS**

108 **Heterochromatin markers macroH2A1 and H3K27me3 increase during infection.**

109 Nuclear egress of HSV-1 capsids utilizes heterochromatin channels that form in the nuclear
110 periphery. We hypothesized that formation of these heterochromatin channels is dependent on
111 host chromatin markers deposited in specific genomic regions. To test this hypothesis, we first
112 examined the levels of multiple indicators of heterochromatin as measured by mass
113 spectrometry during HSV-1 infection in primary human foreskin fibroblast cells (HFFs) (*3*). HFF
114 cells are commonly used as a model for HSV-1 infection as they represent a common site of

115 infection in humans (*22*). We discovered striking upregulation of heterochromatin markers
116 macroH2A1 and H3K27me3 (Fig 1A and Fig S1A). Proteomics data identified the peptide
117 specific to exon 5 of macroH2A1.2, although other peptides detected as increasing may belong
118 to both isoforms of macroH2A1. Therefore, using antibodies specific to each isoform, we
119 examined the levels of macroH2A1.1 and macroH2A1.2 by western blot and found that both
120 isoforms increase during HSV-1 infection (Fig 1A). We also examined macroH2A2 levels and
121 found that they did not change during infection, indicating that changes to macroH2A1 levels are
122 distinct. Since both isoforms of macroH2A1 increase during infection, herein we refer to
123 macroH2A1 as including both macroH2A1.1 and macroH2A1.2. To determine whether these
124 results were specific to fibroblasts cells, we also examined macroH2A1 and macroH2A2 levels
125 during infection in another diploid cell line, retinal pigment epithelial cells (RPEs), which also
126 represent commonly infected cell types (*23*). We found that macroH2A1 levels, but not
127 macroH2A2, also increase in RPE cells during infection (Fig S1B). To define the impact of these
128 heterochromatin markers during HSV-1 infection, we next examined their genomic localization
129 during infection.

130 **MacroH2A1 and H3K27me3 bind broad regions of the host genome that change**
131 **dynamically during HSV-1 infection**

132 We next hypothesized that macroH2A1 is deposited at specific genomic loci on the host
133 genome during infection to promote the formation of heterochromatin. To test this hypothesis,
134 we used CUT&Tag to profile the genomic localization of macroH2A1 at 4, 8 and 12 hours post
135 infection (hpi) in wild-type hTERT-immortalized HFF cells (HFF-T) cells. As a control, we used
136 CRISPR-Cas9 to knock-out (KO) expression of the *macroH2A1* gene in HFF-T cells, which
137 resulted in the loss of macroH2A1.1 and macroH2A1.2, termed macroH2A1 KO cells. We also
138 examined the chromatin profile of H3K27me3 under these conditions to define the genomic
139 heterochromatin landscape. We used *E. coli* DNA as a spike-in to normalize all datasets. On the
140 human genome, we observed clear enrichment of H3K27me3 and macroH2A1 compared to IgG
141 in WT cells (Fig S1C-D). MacroH2A1 CUT&Tag enrichment is below that of IgG in macroH2A1
142 KO cells, but H3K27me3 enrichment is similar to WT, indicating that globally, CUT&Tag worked
143 as expected (Fig S1C-D). In contrast, the macroH2A1 CUT&Tag on the viral genome showed
144 similar enrichments in both WT and macroH2A1 KO cells, indicating that CUT&Tag was not
145 reporting on the protein enrichments on the viral genomes, and there was a significant
146 background signal from the viral genome that couldn't be accounted for (Fig S1I-J). Hence, we
147 focused our analysis on the host genome.

148 On the human genome, we observed large domains of macroH2A1 and H3K27me3 that were
149 gained upon viral infection (Fig 1B). Since large regions are not amenable to traditional peak-
150 based analysis, we instead used domain-based analysis. We partitioned all chromosomes into
151 domains of macroH2A1: domains had an enrichment that was two times the genome-wide
152 median and at least four-fold higher than the IgG control. With the minimum domain size of 1 kb,
153 we observed ~50,000 H3K27me3 domains and ~70,000 macroH2A1 domains genome-wide
154 (Fig S1E). We observed less than 10 macroH2A1 domains in the datasets generated from
155 macroH2A1 KO cells, indicating that our algorithm was identifying robust domains. We then
156 calculated the change in enrichments of macroH2A1 domains during the time course of
157 infection. We performed k-means clustering of the change in macroH2A1 enrichment in
158 macroH2A1 during the time course of infection compared to mock to identify patterns of
159 macroH2A1 gain or loss during infection. With k=6, we observed two clusters to substantially
160 gain macroH2A1 over the course of infection (Clusters 5 and 6, Fig 1C left, Fig S1F). Clusters 1-
161 3 had significant decreases in macroH2A1, whereas cluster 4 had a minor increase (Fig 1C left,
162 Figure S1F). We then asked how these macroH2A1-defined clusters behaved with respect to
163 H3K27me3. Surprisingly, the overall trends across the clusters were preserved in H3K27me3
164 (Fig 1C middle, Fig S1G), though the gains were not as high as macroH2A1. This indicated to
165 us that multiple forms of heterochromatin were gained at specific genomic loci due to viral
166 infection. We then asked if H3K27me3 increases were driven by macroH2A1 deposition. We
167 plotted the H3K27me3 changes at the same clusters for macroH2A1 KO cells (Fig 1C right, Fig
168 S1H). Surprisingly, the trends of H3K27me3 gain/loss were similar between WT and
169 macroH2A1 cells, pointing to the possibility that an upstream event during infection triggers
170 formation of new heterochromatin domains that contain both macroH2A1 and H3K27me3.
171 Furthermore, this upstream event is not affected by loss of macroH2A1. In summary, viral
172 infection results in formation of new heterochromatin domains that span ~10-100s of kilobases.

173 Heterochromatin formation is intimately tied to transcription: chromatin states influence
174 transcription and *vice versa*. Hence, we asked if we could observe changes in transcription that
175 corresponded to gain/loss of heterochromatin during infection. We performed RNA-seq on WT
176 and macroH2A1 KO cells over the course of infection and calculated fold changes in RNA levels
177 at each time point over the mock control. We identified genes that intersected with domains in
178 each cluster defined in Figure 1C and plotted the distribution of RNA fold changes of the genes
179 grouped by the clusters to which they belonged. We observed the change in RNA to anti-
180 correlate with change in macroH2A1: clusters 1-3 had an increase in RNA levels, whereas

181 clusters 4-6 had a decrease in RNA levels over the course of infection (Fig 2A). To determine
182 the order of events, that is if the gain in macroH2A1 leads to decreased transcription or if
183 decreased transcription leads to gain in macroH2A1, we performed the same analysis in
184 macroH2A1 KO cells. Strikingly, the gene expression changes in macroH2A1 KO cells mirror
185 that of WT cells, leading us to conclude that transcriptional changes are upstream of
186 macroH2A1 deposition (Fig 2B).

187 Steady state RNA changes could occur both due to changes in transcription and changes in
188 RNA decay. For changes in global RNA levels to cause changes in chromatin state, the most
189 direct connection would be via changes in transcription: transcription increases nucleosome
190 turnover (*24*) and counteracts heterochromatin formation and/or maintenance (*25*). Hence, we
191 asked if changes in RNA reflected changes in transcription. We analyzed published 4sU-RNA-
192 labeling data over the time course of infection (*26*) and found that the changes at 8hpi largely
193 followed the same trend as the total RNA: clusters 1-3 featured increased transcription, whereas
194 clusters 5 and 6 featured decreased transcription during infection (Fig 2C). Interestingly, cluster
195 4 diverged between total RNA and 4sU-RNA data: 4sU-RNA increased whereas total RNA
196 decreased. This indication of active transcription explains why cluster 4 features a weak
197 macroH2A1 gain.

198 Finally, we asked if the gain or loss of macroH2A1 happened across previously defined genome
199 compartments (*27*). We determined the distribution of the eigenvector corresponding to A/B
200 compartments for IMR90 Hi-C data from the 4DN project (*28*). Here, positive values correspond
201 to the A compartment, which features higher gene density and accessible chromatin, whereas
202 negative values correspond to the B compartment, which features inactive chromatin. All
203 clusters except cluster 2 are significantly biased towards one of the compartments: clusters 1
204 and 3 are significantly biased towards compartment B, whereas clusters 4-6 are significantly
205 biased towards compartment A (Fig 2D). Strikingly, the median of the clusters increases moving
206 from Cluster 1 to Cluster 6, correlating with macroH2A1 gain upon infection. Thus, macroH2A1
207 gains and losses happen in distinct genomic compartments upon viral infection. In summary,
208 decreased transcription in specific regions in compartment A due to viral infection causes gain
209 in macroH2A1 at these same regions and the gains in macroH2A1 are mirrored by gains in
210 H3K27me3. Taken together, these data suggest that macroH2A1 and H3K27me3 function to
211 form new regions of repressed chromatin on the host genome during HSV-1 infection.
212 Therefore, we next examined infection progression in the absence of these markers.

213 **Loss of macroH2A1 results in reduced viral progeny but does not affect genome or**
214 **protein accumulation**

215 To investigate the role of macroH2A1 in HSV-1 infection, we infected WT and macroH2A1 KO
216 HFF-T cells with HSV-1. Our CRISPR-Cas9 disruption of macroH2A1 resulted in loss of both
217 macroH2A1.1 and macroH2A1.2, but not macroH2A2 (Fig 3A). Upon infection, we examined
218 viral protein accumulation and observed similar levels of ICP0 (immediate early (*29*)), VP16
219 (early (*30*)) and glycoprotein H (gH, late (*31*)) in both wild type (WT) and macroH2A1 KO cells
220 (Fig 3A). We next examined HSV-1 replication and measured viral genome accumulation by
221 droplet digital PCR (ddPCR). We observed no significant difference in viral genome
222 accumulation between WT and macroH2A1 KO cells (Fig 3B), indicating that neither HSV-1
223 replication nor protein production is affected by macroH2A1 loss. To determine the impact of
224 macroH2A1 loss on viral progeny production, we measured viral genome accumulation in the
225 supernatant. We discovered a 6-fold decrease in the levels of HSV-1 genomes produced in the
226 supernatant of macroH2A1 KO cells compared to those produced from WT cells at 12 hpi (Fig
227 3C). We further discovered that infectious progeny produced from infected macroH2A1 KO cells
228 were significantly decreased compared to those produced from WT cells at 8 and 12 hpi (Fig
229 3D). To determine whether these effects held true in multiple cell types, we also infected
230 macroH2A1 KO RPE cells and found similar viral protein accumulation compared to control cells
231 (Fig S2A). Viral titers produced from macroH2A1 KO RPE cells were also significantly lower
232 than those produced from control cells (Fig S2B), consistent with our results in HFF-T cells.
233 Importantly, we also quantified total viral RNA via RNA-seq and determined that there were no
234 significant changes in viral RNA accumulation between WT and macroH2A1 KO cells (Fig S2C),
235 consistent with our measurements of protein and genome accumulation. Taken together, these
236 data indicate that loss of macroH2A1 leads to a significant defect in viral progeny but not
237 protein, RNA, or genome accumulation. Therefore, we conclude that macroH2A1 is important
238 for HSV-1 egress.

239 **Depletion of H3K27me3 also results in reduced viral progeny**

240 Given our observation that both macroH2A1 and H3K27me3 levels increase during HSV-1
241 infection (Fig S1A), we hypothesized that H3K27me3 is also important for viral egress.
242 Therefore, we investigated how reduction of H3K27me3 would impact HSV-1 infection. To
243 reduce H3K27me3 levels, we targeted the EZH2 enzyme that deposits this mark (*32*) using an
244 inhibitor called Tazemetostat or “Taz” (EPZ-6438) (*33*). We treated cells with 10 μM of Taz or

245 DMSO control for 3 days to allow for reduction of H3K27me3 and then infected with HSV-1 (Fig
246 3E). We treated both WT and macroH2A1 KO cells to examine any synergistic effects of these
247 two heterochromatin markers. Consistent with mass spectrometry measurements, we observe
248 an increase in H3K27me3 levels as infection progresses (comparing 4, to 8 to 12hpi), although
249 the mock levels are higher than those at 4 hpi. This increase during infection is also observed in
250 the macroH2A1 KO cells, suggesting that it is not dependent on the presence of macroH2A1.
251 We found that accumulation of viral proteins ICP0, VP16 and gH were not affected by the
252 reduction of H3K27me3 (Fig 3E). Further, we observed that the reduction of H3K27me3 in
253 macroH2A1 KO cells also did not impact accumulation of these viral proteins at 4, 8 or 12hpi
254 (Fig 3F). We next examined viral genome accumulation and found that reduction of H3K27me3
255 resulted in a modest but significant 2-fold decrease in viral genome accumulation within cells
256 (Fig 3G, grey bars). We observed no additional decrease in viral genomes in macroH2A1 KO
257 cells treated with the inhibitor, suggesting that regardless of H3K27me3 levels, loss of
258 macroH2A1 does not impact viral replication as we observed above (Fig 3G, pink bars). We
259 next measured viral genomes in the supernatant to determine the impact of H3K27me3
260 reduction on progeny production and found a significant 4-fold decrease at 12 hpi from inhibitor-
261 treated cells compared to DMSO-treated (Fig 3H). Further, we found infectious progeny
262 produced from inhibitor-treated cells were significantly reduced at 12 hpi compared to those
263 produced from control cells (Fig 3I). Interestingly, H3K27me3 reduction in macroH2A1 KO cells
264 does not result in an additional defect in progeny production, suggesting the two markers
265 function in the same genetic pathway. Importantly, the modest decrease in viral replication
266 produced from cells lacking H3K27me3 does not fully explain the greater reduction in progeny,
267 suggesting that H3K27me3 is also important for HSV-1 egress. These results are consistent
268 with a previous report that found HSV-1 titers, but not viral replication, were reduced upon EZH2
269 inhibition (*34*). Furthermore, we did not observe any significant differences in the ratio of
270 genomes to plaque forming units (pfu) upon loss of macroH2A1, H3K27me3, or both, compared
271 to control conditions (Fig S2D), indicating that loss of these markers does not result in
272 significantly more defective particles. Taken together, these results indicate that H3K27me3 is
273 also important for efficient viral egress.

274 **MacroH2A1-dependent heterochromatin in the nuclear periphery is critical for efficient**
275 **HSV-1 nuclear egress**

276 HSV-1 capsids in the nucleus access the nuclear membrane through channels bracketed by
277 highly dense chromatin at the nuclear periphery (*4*, *6*, *35*). We found that loss of macroH2A1 or

278 depletion of H3K27me3 results in decreased viral progeny but has no or minimal impact on viral
279 replication. Therefore, we hypothesized that efficient HSV-1 egress out of the nuclear
280 compartment requires macroH2A1- or H3K27me3-dependent heterochromatin in the nuclear
281 periphery. Because loss of macroH2A1 resulted in no effect on viral replication compared to a
282 modest effect produced by inhibition of H3K27me3 deposition, we chose to focus on
283 macroH2A1 KO cells for heterochromatin visualization. We used transmission electron
284 microscopy (TEM) to image nuclei and examined heterochromatin formation in uninfected cells
285 (Fig 4A). We found that macroH2A1 KO cells had strikingly less heterochromatin in the nuclear
286 periphery than WT cells. This is consistent with what has been reported for hepatoma cells upon
287 loss of macroH2A1 and macroH2A2 (*15*). We quantified the width of heterochromatin at the
288 nuclear periphery in each cell type through binary thresholding of the intensity of electron-dense
289 regions and found that loss of macroH2A1 results in a significant reduction in peripheral
290 heterochromatin (Fig 4B). To test how this loss of macroH2A1-dependent heterochromatin
291 impacts HSV-1 nuclear egress, we infected these cells and quantified capsids in the nucleus
292 (Fig 4C-D and S3). Consistent with previous reports, in WT cells we found HSV-1 capsids
293 egressing through heterochromatin channels (Fig 4C and Fig S3B). We found that infected
294 macroH2A1 KO nuclei have significantly more HSV-1 capsids than those of WT cells (Fig 4D),
295 indicating that loss of macroH2A1-dependent heterochromatin is detrimental for efficient nuclear
296 egress. Herpesvirus infection produces three subtypes of capsids: A capsids which are empty,
297 B capsids which contain scaffolding proteins, and C capsids which contain viral gDNA and are
298 considered the precursor to infectious virions (*36*, *37*). To determine whether nuclear egress or
299 capsid formation is dependent on heterochromatin channels, we quantified the proportion of
300 each capsid type in WT and macroH2A1 KO cells. We found no difference in the proportion of
301 each capsid type between the two cell types (Fig S3C-D). Taken together, these data indicate
302 that macroH2A1-dependent heterochromatin in the nuclear periphery is critical for efficient
303 nuclear egress.

304 **Clinical isolates of HSV-1 also require macroH2A1 for efficient egress**

305 Our results above were generated using a lab adapted strain of HSV-1 (*syn 17*+), which may
306 not accurately represent a naturally occurring virus. Therefore, we decided to test whether
307 clinical isolates of HSV-1 would also be affected by loss of heterochromatin. We infected WT
308 and macroH2A1 KO cells with HSV-1 categorized as isolated from “low-shedding” or “high-
309 shedding” patients. We measured protein accumulation at 4, 8, and 12 hpi and viral genome
310 accumulation in cells and supernatant by ddPCR. We found that there was no significant

311 change in viral protein or viral genome accumulation for either clinical isolate in macroH2A1 KO
312 cells (Fig 5A-B). We measured viral genomes in the supernatant and found that there was a
313 modest reduction in HSV-1 genomes in the supernatant of macroH2A1 KO cells compared to
314 control cells (Fig 5C). For both clinical isolates, we found that macroH2A1 KO cells produced
315 significantly fewer progeny than WT cells at 12 hpi (Fig 5D). Taken together, these results
316 indicate that egress of clinically isolated HSV-1 is also dependent on macroH2A1.

317 **DISCUSSION**

318 Host chromatin is emerging as a critical barrier to viral success. Elegant electron microscopy
319 work showed that during HSV-1 infection, host chromatin is marginalized to the nuclear
320 periphery (*2*, *6*). Viral capsids subsequently egress through regions of less dense staining
321 termed heterochromatin channels (*35*). We found that markers of heterochromatin macroH2A1
322 and H3K27me3 were upregulated during HSV-1 infection. Therefore, we hypothesized that
323 these markers are critical for the formation of heterochromatin channels in the nuclear periphery
324 that allow for efficient viral egress from the nuclear compartment. Here, we showed that
325 macroH2A1 and H3K27me3 bind broad regions of the host genome which correlate with
326 decreased transcription, indicative of heterochromatin. Furthermore, we find that these regions
327 are primarily found in transcriptionally active compartments defined by Hi-C, supporting the idea
328 that newly formed heterochromatin increases during HSV-1 infection. However, the
329 mechanisms by which macroH2A1 and H3K27me3 are upregulated are still unclear. One recent
330 study showed that changes in chromatin accessibility during HSV-1 infection were akin to those
331 observed during heat shock or salt stress (*38*). Further, H3K27me3 is often deposited as a
332 consequence of transcriptional changes rather than the cause (*39*). We find that H3K27me3 is
333 still increased in large genomic regions (clusters 5-6) in the absence of macroH2A1 (Fig 1),
334 suggesting that it is deposited independently of macroH2A1. Taken together with published
335 findings, our study suggests that a global host response to the stress of infection results in a
336 decrease in transcription of many genes and thus increased macroH2A1 and H3K27me3-
337 dependent heterochromatin. This increased heterochromatin is then exploited by the virus as a
338 structure through which newly formed capsids can traverse to access the inner nuclear
339 membrane and egress (Fig 5E).

340 We found that loss of macroH2A1 or depletion of H3K27me3 resulted in significantly reduced
341 infectious progeny (Fig 3). Interestingly, we found that depletion of H3K27me3, but not loss of
342 macroH2A1, results in a modest but significant decrease in viral genome accumulation

343 compared to control cells. Because we did not detect H3K27me3 on viral genomes, consistent
344 with a recent study that detected very low levels (*40*), it is possible that inhibiting the deposition
345 of this mark has other effects in the cell. Indeed, this agrees with the complex effects observed
346 when multiple EZH1/2 inhibitors were compared in a recent study (*34*). They found treatment
347 with EZH1/2 inhibitors induced a cellular antiviral state that also suppressed infection with
348 multiple DNA and RNA viruses. Furthermore, proteomics revealed that other heterochromatin
349 marks like H3K9me3 are also changing during HSV-1 infection (*3*), suggesting that there may
350 be other mechanisms of heterochromatin dynamics at play. It will be interesting to consider the
351 diverse implications of heterochromatin domains not only as a means of transcriptional
352 regulation but also as a structural component that impacts many aspects of viral infection.

353 Using transmission electron microscopy, we showed that loss of macroH2A1 results in
354 decreased heterochromatin in the nuclear periphery. Our results echo those found in Hep2G
355 cells where loss of macroH2A1 and macroH2A2 was shown to cause significant disruption of
356 heterochromatin in the nuclear periphery (*15*). It is possible that the presence of macroH2A2 in
357 our macroH2A1 KO cells compensates to some degree, although we do not see any changes in
358 macroH2A2 either upon loss of macroH2A1 or during infection suggesting the upregulation
359 phenotype of macroH2A1 is distinct. It is also possible that different cell types have varying
360 degrees of dependence on macroH2A1-enriched heterochromatin that we are only beginning to
361 discern. We used HFFs and RPEs to test our hypothesis, however, in both cases we used
362 hTERT-immortalized diploid cells. MacroH2A1 was also reported to regulate telomere
363 maintenance (*41*), suggesting a threshold of macroH2A1 may be required for cell survival. Our
364 CUT&Tag data indicate that while macroH2A1 is enriched in large regions defined in clusters 5
365 and 6, we also observe a decrease in clusters 1-3. This suggests that detecting a global
366 increase in total levels of macroH2A1 may be variable. Indeed, we observed that infected
367 primary HFFs consistently showed an increase in macroH2A1 while HFF-T cells infected with
368 clinical isolates of HSV-1 did not. Furthermore, as the heatmaps in Figure 1 indicate, large
369 regions of the genome are both losing and gaining macroH2A1 and H3K27me3 during infection.
370 Taken together, it is clear that other factors regulate macroH2A1 levels and future work to
371 determine the mechanism of upregulation as a response to infection will further define the host
372 response.

373 Our electron microscopy revealed greater numbers of capsids trapped in the nucleus of
374 macroH2A1 KO cells. Our analysis uncovered that the proportion of capsid type was not
375 different in WT compared to macroH2A1 KO cells (Fig S3C-D), suggesting that heterochromatin

does not play a role in capsid formation but rather acts as a structural highway for formed capsids to reach the inner nuclear membrane. At the inner nuclear membrane, capsids are aided by the nuclear egress complex, comprised of viral proteins UL34 and UL31, to bud into the inner nuclear membrane and fuse with the outer nuclear membrane for further maturation steps in the cytoplasm (*42*). Multiple reports describe that not only does lamina disruption occur independently of capsid formation, but that chromatin is likely the limiting factor in viral egress (*43–48*). Taken together, our results demonstrate that macroH2A1 and H3K27me3- dependent heterochromatin is exploited by HSV-1 to efficiently egress from the nuclear compartment.

AUTHOR CONTRIBUTIONS

Conceptualization, H.C.L, L.K.M., and D.C.A; methodology H.C.L, L.K.M., and D.C.A.; formal analysis, H.C.L, L.K.M., S.R., and D.C.A.; investigation, H.C.L, L.K.M., M.R.B., H.E.A, E.E.A, and D.C.A; resources, H.C.L, L.K.M., M.R.B., H.E.A, E.E.A, S.R., and D.C.A.; data curation, H.C.L, L.K.M., M.R.B., S.R., and D.C.A.; writing – original draft, H.C.L, L.K.M., M.R.B., S.R., and D.C.A.; writing – review & editing, H.C.L, L.K.M., M.R.B., H.E.A, E.E.A, S.R., and D.C.A.; visualization, H.C.L, L.K.M., S.R., and D.C.A.; supervision, H.C.L, L.K.M., and D.C.A.; funding acquisition, H.C.L., E.A.A, S.R., and D.C.A.

ACKNOWLEDGEMENTS

We thank members of the Avgousti lab, M. Emerman, A. Geballe, M. Lagunoff, K. Lynch, S. Parkhurst, and M. Weitzman for insightful comments. We thank D. Janssens and the Henikoff lab for reagents and assistance with CUT&Tag. We thank the Salama and Overbaugh labs for assistance with ddPCR. We thank the Jerome lab for the clinical HSV isolates and the Cellular Imaging, Electron Microscopy (EMSR), F. Wu and Genomics & Bioinformatics Shared Resource Facilities at the Fred Hutchinson Cancer Research Center for help with sequencing and data analysis. We thank J. Dubrulle and the Cellular Imaging Shared Resource (CISR) for help with image analysis. The EMSR, CISR, and Genomics core are supported in part by the Fred Hutch/University of Washington Cancer Consortium (P30 CA015704). This study was supported by start-up funds from the RNA Bioscience Initiative at the University of Colorado School of Medicine (S. R.), the Fred Hutch (D.C.A.), and NIH funding to H.C.L. (AI083203), E.A.A. (AI083203), S.R. (GM133434), and D.C.A. (GM133441).

409 **FIGURES**

Figure 1. MacroH2A1 and H3K27me3 increase during lytic HSV-1 infection and form broad chromatin regions.

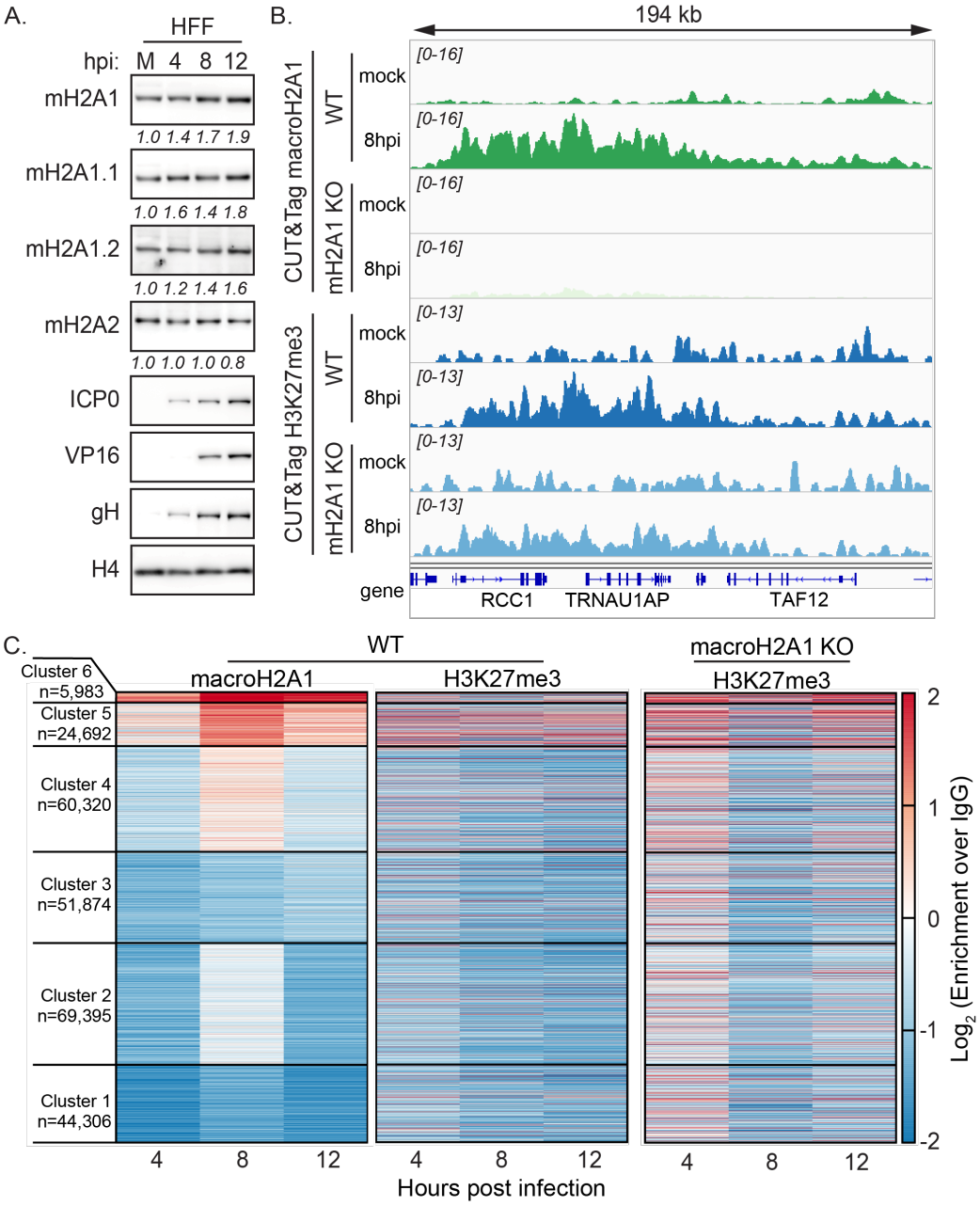

410

411 **Figure 1. MacroH2A1 and H3K27me3 increase during lytic HSV-1 infection and form**

412 **broad chromatin regions.**

413 A. Western blot of total macroH2A1 (mH2A1), mH2A1.1, mH2A1.2 and mH2A2 with

414 relative quantification below indicated blots during HSV-1 infection showing mock

415 infected (M), 4-, 8-, and 12-hours post-infection (hpi) in primary HFFs. ICP0, VP16, gH
416 are shown as representative HSV-1 proteins. H4 is a loading control.
417 B. Representative genome browser snapshots of spike-in normalized CUT&Tag enrichment
418 of macroH2A1 and H3K27me3 showing increases at 8hpi of HSV-1 infection as
419 measured by CUT&Tag in WT or macroH2A1 KO as indicated. The region
420 corresponding to chromosome 1, 28,500 kb to 28,660 kb, is shown.
421 C. Changes in log2 enrichment of spike-in normalized CUT&Tag of macroH2A1 and
422 H3K27me3 over IgG compared to mock treatment are shown as a heatmap. Each line in
423 the heatmap represents a domain of macroH2A1.

424

Figure 2. MacroH2A1 and H3K27me3 presence correlates with decreased transcription.

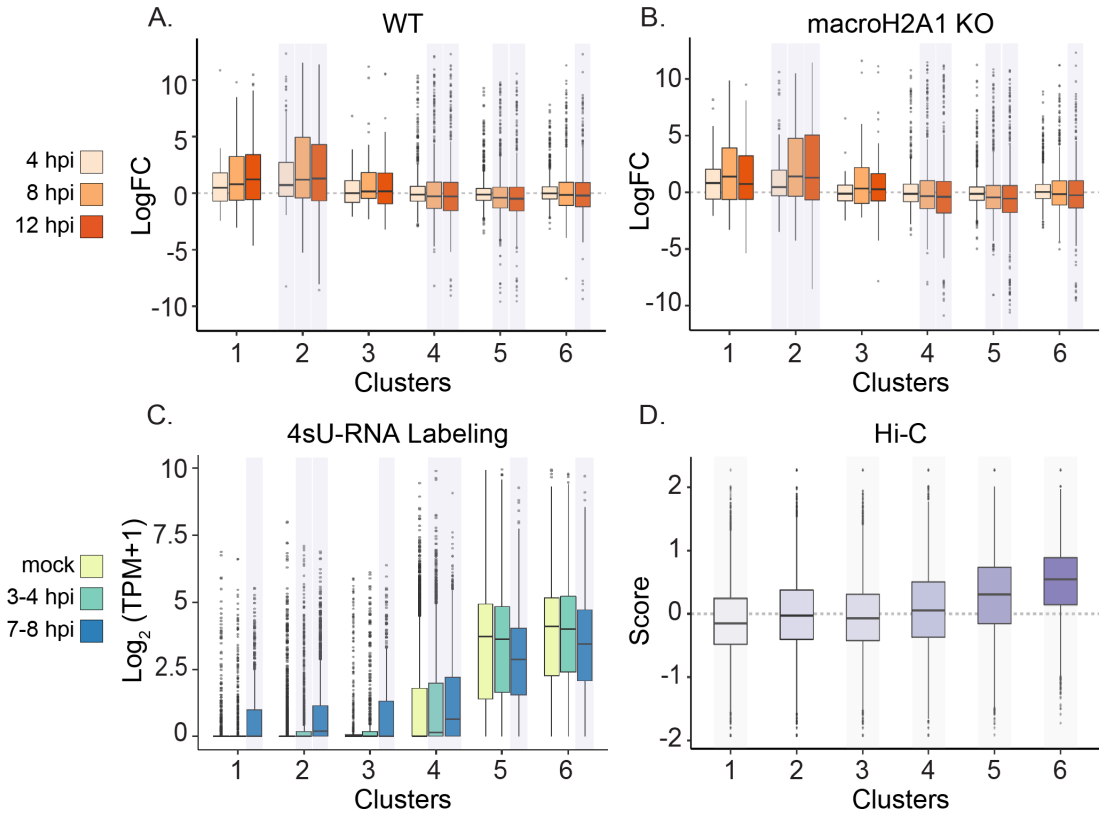

Figure 2. MacroH2A1 and H3K27me3 presence correlates with decreased transcription.

A. Box plots of total host RNA from RNA-seq for genes overlapping clusters from Figure 1. Kolmogrov-Smirnov test (in R) was performed comparing logCPM values of genes at each time point with logCPM values of genes from mock dataset for each cluster. The p-values were corrected for multiple testing, and the time points and clusters with corrected p-value less than 0.05 are shaded.

B. Same as A for macroH2A1 KO cells.

C. 4sU-RNA counts for genes from Hennig *et al* (*38*) overlapping with clusters from Figure 1 shown as box plots and shading as indicated in (A).

D. Box plots of Hi-C eigenvector scores of regions overlapping with clusters from Figure 1. The Hi-C compartment eigen vector scores were obtained from 4DN project website. Wilcoxon signed rank test with alternate hypothesis that the true location is not equal to 0 was performed on the distribution of eigen vector scores for each cluster. The p-values

were corrected for multiple testing, and the clusters with corrected p-value less than 0.05 are shaded. Bonferroni correction was used for p-value adjustments.

Figure 3. MacroH2A1 and H3K27me3 are required for efficient HSV-1 egress.

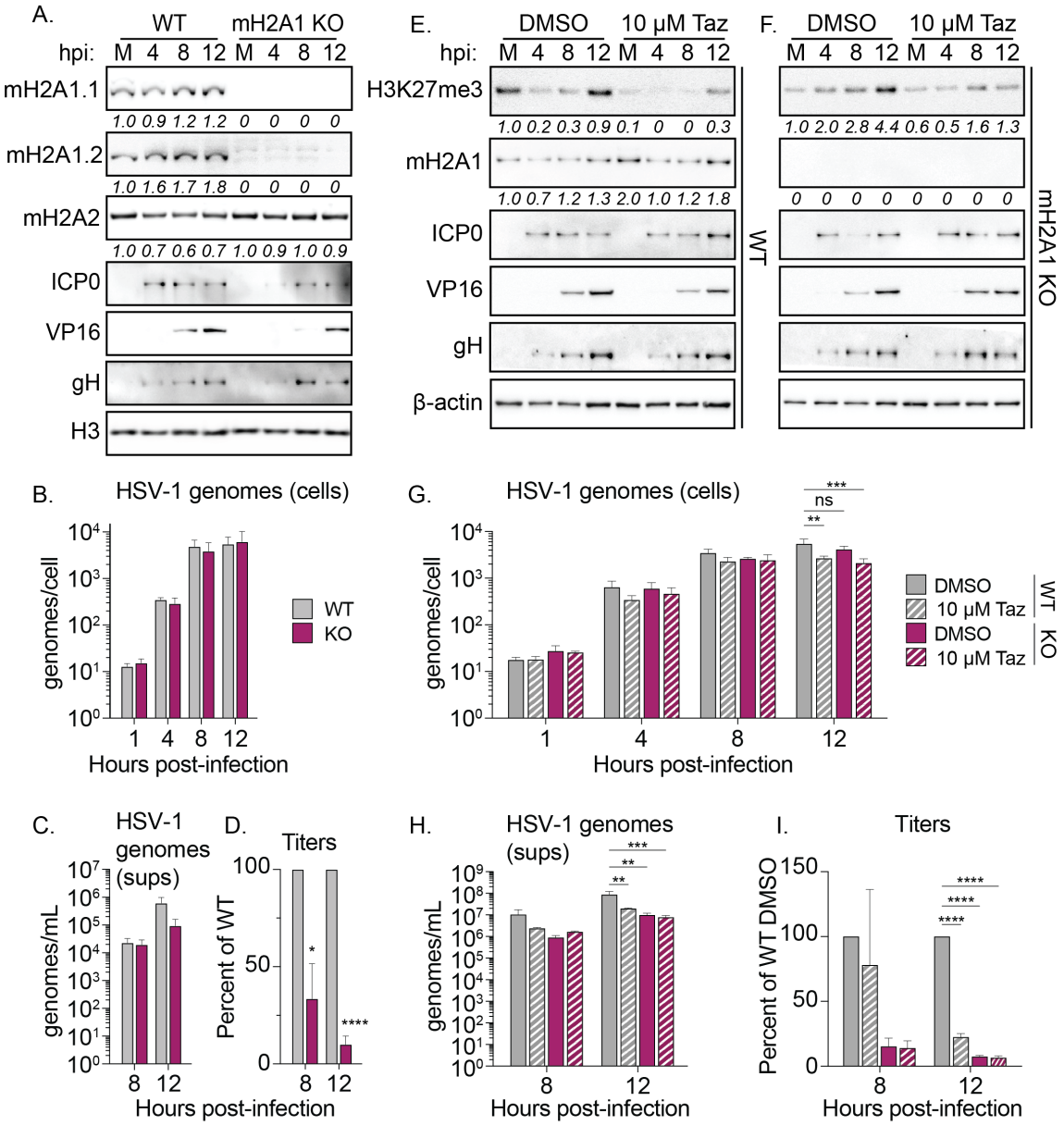

Figure 3. MacroH2A1 and H3K27me3 are required for efficient HSV-1 egress.

A. Western blot of total macroH2A1 (mH2A1), mH2A1.1, mH2A1.2 isoforms and mH2A2 during HSV-1 infection. Mock infected (M), 4-, 8-, and 12-hours post-infection in WT and macroH2A1 knockout (mH2A1 KO) HFF-Ts are shown as indicated. Quantification of relative intensity is shown below indicated blots and H3 is shown as a loading control.

454 B. Droplet digital (ddPCR) quantification of HSV-1 genomes extracted from the infected
455 cells as indicated for each time point. Error bars represent the SEM of three biological
456 replicates.
457 C. ddPCR quantification of HSV-1 genomes released from WT or mH2A1 KO cells and
458 isolated from supernatants (sups). Error bars represent the SEM of three biological
459 replicates.
460 D. Infectious progeny produced by WT or mH2A1 KO cells quantified by plaque assay. Viral
461 yield is indicated as the percent yield compared to WT and was calculated by dividing
462 plaque-forming units (pfu) per mL of the mH2A1 knockout titers by the WT titers of each
463 respective virus at indicated time points. * p. < 0.05, **** p < 0.0001.
464 E. Western blot of H3K27me3 and mH2A1 during HSV-1 infection shown as mock infected
465 (M), 4-, 8-, and 12-hours post-infection. WT cells were pretreated with DMSO or
466 tazemetostat inhibitor (Taz) for 3 days prior to infection and remained with inhibitor over
467 the course of infection. Beta-actin is shown as a loading control. Quantification of relative
468 intensity over beta-actin normalized to the mock sample on the same blot are shown.
469 F. Western blot as in E for macroH2A1 KO cells.
470 G. Infection as in E. ddPCR quantification of HSV-1 genome accumulation as in B. Error
471 bars represent the SEM of three biological replicates. ** p < 0.01, *** p < 0.001.
472 H. Infection as in E and F with quantification as in C comparing HSV-1 genomes released
473 from Taz or DMSO treated WT or mH2A1 knockout. Error bars represent the SEM of
474 three biological replicates. ** p < 0.01, *** p < 0.001.
475 I. Infection as in E and F quantifying infectious progeny produced by WT or mH2A1
476 knockout cells with DSMO or Taz pretreatment by plaque assay. Viral yield is indicated
477 as the percent yield compared to WT as in D. **** p < 0.0001.

478

479

Figure 4. HSV-1 requires macroH2A1-dependent hetero-
chromatin for efficient egress.

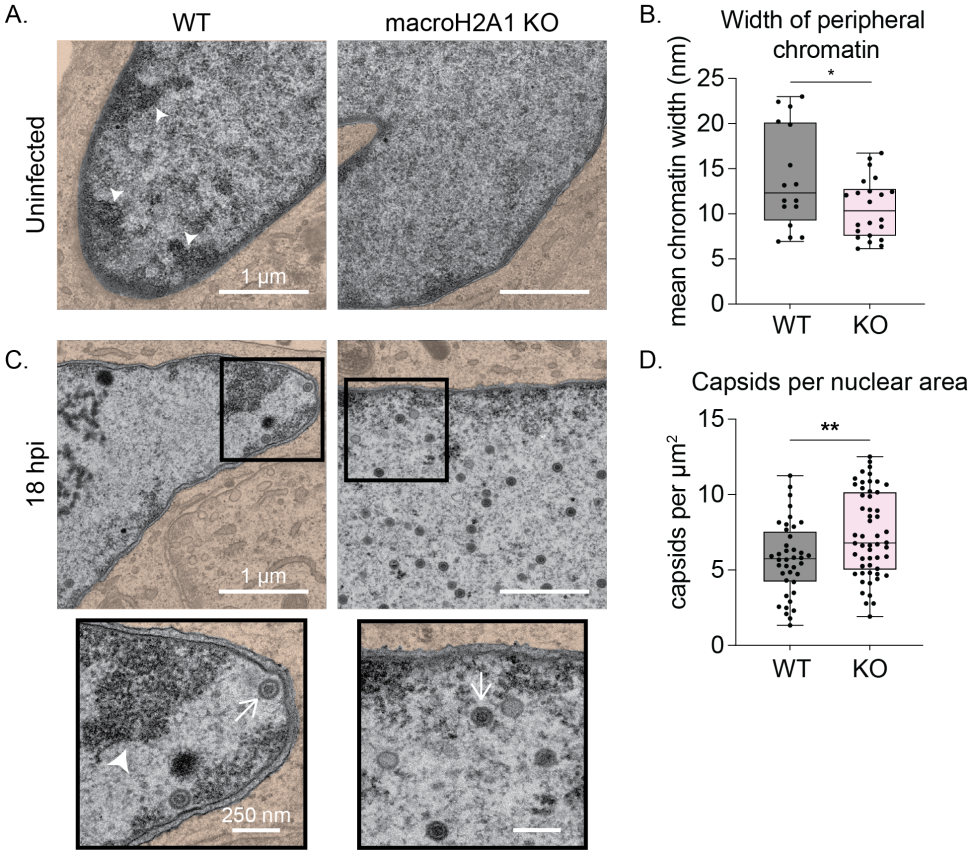

Figure 4. HSV-1 requires macroH2A1-dependent heterochromatin for efficient egress.

A. Transmission electron microscopy (TEM) images of representative nuclei of uninfected WT (left) or macroH2A1 KO (right) cells. Regions outside of the nucleus are colorized orange. Dark regions (arrowhead) represent high density heterochromatin. Scale bar is 1µm.

B. Quantification of peripheral heterochromatin width in uninfected nuclei from A. Width was measured in nm from the nuclear periphery via binary thresholding from intensity profiles sampled every 10 pixels. Mean width was plotted for each nucleus. $p < 0.05$ (n=16 WT, n=22 macroH2A1 KO).

C. TEM images of representative WT and macroH2A1 knockout nuclei at 18 hours post-infection with HSV-1. Insets show enlarged views of respective boxed areas containing

493 capsids within nuclei with scale bars as indicated. Arrowhead indicates heterochromatin,
494 arrow indicates viral capsid.
495 D. Quantification of all capsids within nuclei from C. Number of capsids was normalized
496 according to nucleus area in μm^2. $p < 0.01$ (n=40 WT, n=55 mH2A1 KO).
497
498
499

Figure 5. MacroH2A1 is required for egress of clinical HSV-1 isolates.

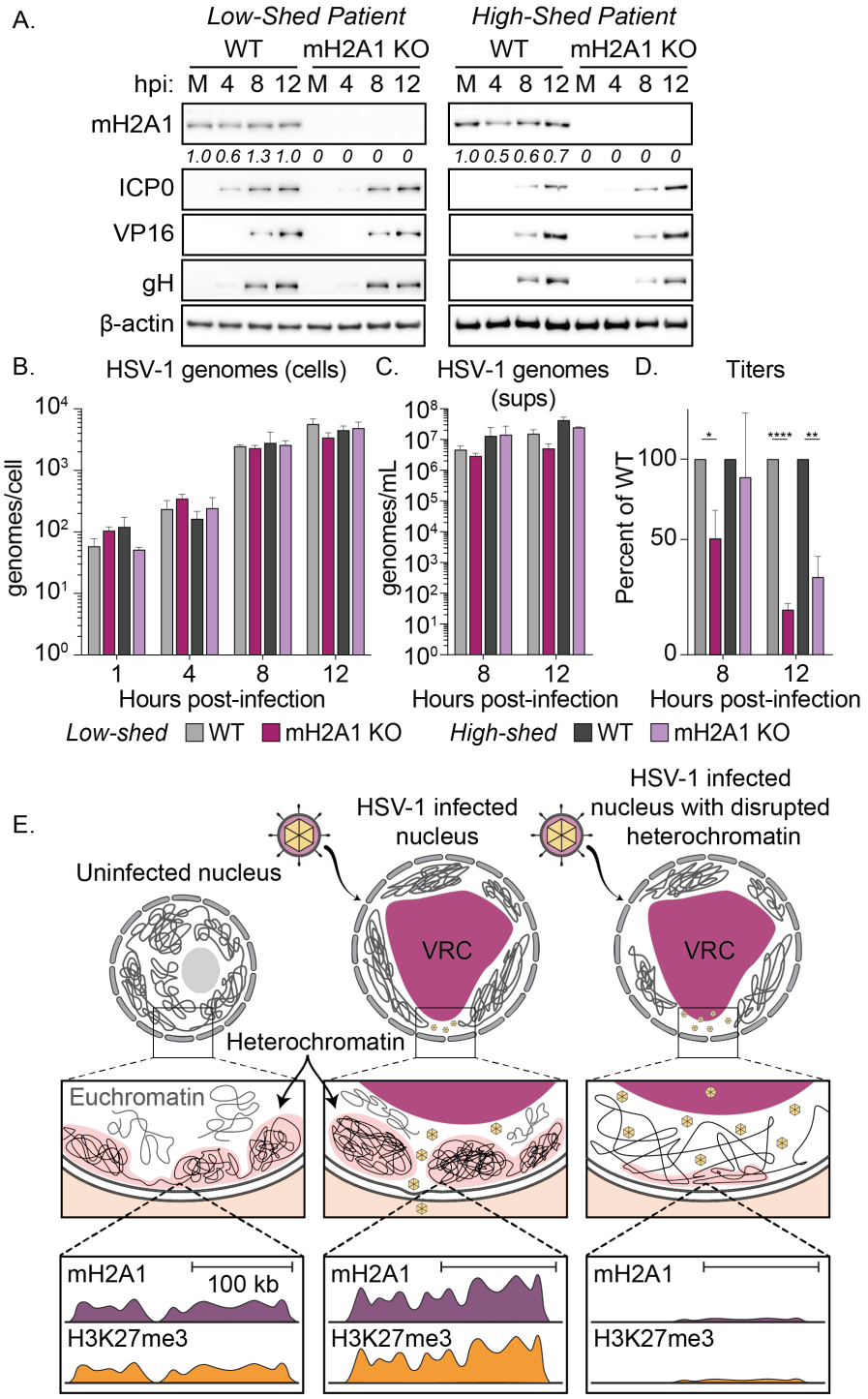

Figure 5. MacroH2A1 is required for egress of clinical HSV-1 isolates.

A. (A-D) WT or macroH2A1 (mH2A1) KO HFF-T were mock-infected (M) or infected with a low-shedding or high-shedding clinical HSV-1 isolate as indicated for 1, 4, 8 and/or 12

505 hours. Western blots of proteins as indicate with beta-actin shown as loading control.
506 Fold-change of mH2A1 protein levels normalized to mH2A1 level in mock-infected cells
507 are shown below the indicated blots.
508 B. Infection as in A. ddPCR quantification of HSV-1 genome accumulation within cells.
509 Error bars represent the SEM of three biological replicates.
510 C. ddPCR quantification of HSV-1 genomes released from WT or macroH2A1 knockout
511 cells. Error bars represent the SEM of three biological replicates. * $p < 0.05$.
512 D. Infectious progeny produced by WT or macroH2A1 knockout cells quantified through
513 plaque assay. Viral yield is indicated as the percent yield compared to WT. * p. < 0.05, **
514 $p < 0.01$, **** $p < 0.0001$.
515 E. Model for heterochromatin support of HSV-1 egress. In uninfected cells (left),
516 heterochromatin is enriched in the nuclear periphery. Upon infection with HSV-1
517 (middle), there is an increase in heterochromatin at specific regions in the nuclear
518 periphery that results in formation of heterochromatin channels that allow capsids to
519 traverse from the viral replication centers (VRCs) the inner nuclear membrane where
520 they bud into the perinuclear space and subsequently fuse with the outer nuclear
521 membrane into the cytoplasm. In infected cells missing heterochromatin markers
522 macroH2A1 or H3K27me3 (right), these heterochromatin channels cannot form properly
523 which results in increased capsids trapped in the nuclear compartment.
524
525

526 **SUPPLEMENTAL FIGURES**

Supplemental Figure S1. Quantification of macroH2A1 and H3K27me3 enrichment during HSV-1 infection.

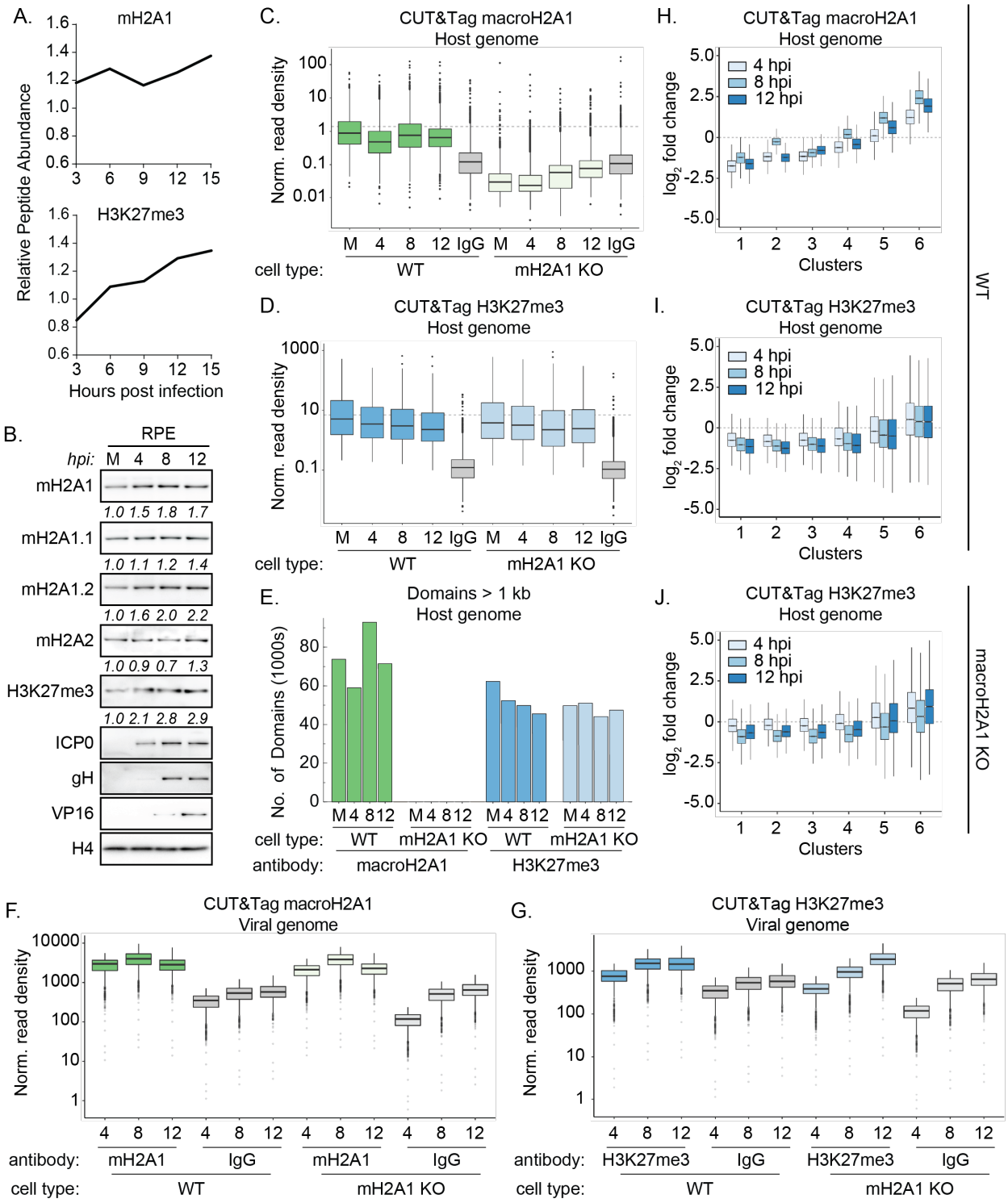

527

528 **Supplemental Figure S1. Quantification of macroH2A1 and H3K27me3 enrichment during**
529 **HSV-1 infection.**

530 A. Relative peptide abundance of total macroH2A1 and H3K27me3 by mass spectrometry
531 over the course of HSV-1 infection in primary HFFs from (*3*). Values shown are
532 normalized to mock levels.
533 B. Western blot of total macroH2A1 (mH2A1), macroH2A1.1, macroH2A1.2, macroH2A2,
534 and H3K27me3 in mock infected (M), and 4-, 8-, and 12-hours post-infection with HSV-1
535 in RPEs. ICP0, VP16, gH are HSV-1 proteins. H4 is shown as a loading control.
536 C. Spike-in normalized, genome-wide CUT&Tag read density of macroH2A1 from WT HFF-
537 T and macroH2A1 KO cellular genomes during HSV-1 infection.
538 D. Spike-in normalized, genome-wide CUT&Tag read density of H3K27me3 on WT HFF-T
539 and macroH2A1 KO cellular genomes during HSV-1 infection.
540 E. Total number of macroH2A1 and H3K27me3 domains over 1 kb as measured by
541 CUT&Tag of WT HFF-T and macroH2A1 KO cell genomes during HSV-1 infection.
542 F. Quantification of heatmaps from Figure 1C showing macroH2A1 enrichment across the
543 clusters.
544 G. Quantification of heatmaps from Figure 1C showing H3K27me3 enrichment in clusters
545 defined by macroH2A1 as in (H).
546 H. Quantification as in (I) in macroH2A1 KO cells.
547 I. Spike-in normalized CUT&Tag read density of macroH2A1 on HSV-1 viral genomes
548 during infection of WT HFF-T and macroH2A1 KO cells.
549 J. Spike-in normalized CUT&Tag read density of H3K27me3 on HSV-1 viral genomes
550 during infection of WT HFF-T and macroH2A1 KO cells.

551

552

553

554

555

Supplemental Figure S2. MacroH2A1 is required for egress but does not impact HSV-1 transcription or particle to genome ratios.

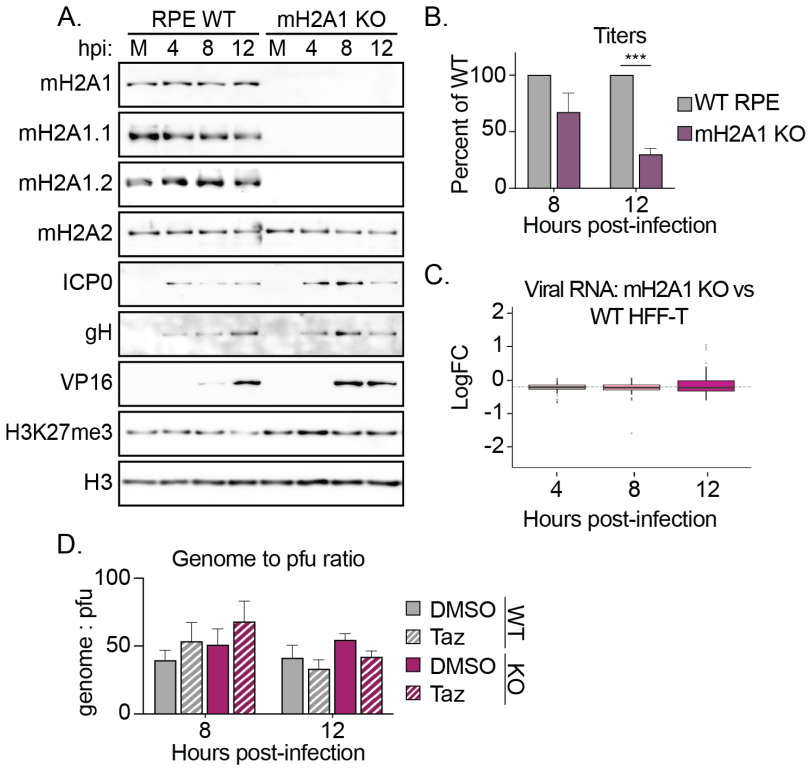

Supplemental Figure S2. MacroH2A1 is required for egress but does not impact HSV-1 transcription or particle to genome ratios.

A. Western blot of total macroH2A1 (mH2A1), macroH2A1.1, macroH2A1.2 and macroH2A2 proteins as indicated in mock infected and 4-, 8-, and 12-hpi with HSV-1 in hTERT-immortalized RPEs and macroH2A1 knockout hTERT-immortalized RPEs. H3 is shown as a loading control.

B. Infectious progeny produced by WT or macroH2A1 knockout RPE cells were quantified by plaque assay. Viral yield is indicated as the percent yield compared to WT and was calculated by dividing pfu per mL of the macroH2A1 knockout titers by the WT titers of each respective virus at each indicated time point. *** $p. < 0.001$.

C. Log2 fold-change of HSV-1 transcripts at 4, 8 and 12 hpi identified by RNA-seq in macroH2A1 KO compared to WT HFF-T cells. There is no significant difference between the cell types.

D. Genome to pfu ratio of HSV-1 in WT or mH2A1 knockout HFF-T cells treated with 10 uM tazemetostat (Taz) or DMSO. Ratio was calculated from the samples used to generate Figure 3H-I. No significance by ANOVA.

Supplemental Figure S3. HSV-1 capsid formation is independent of macroH2A1.

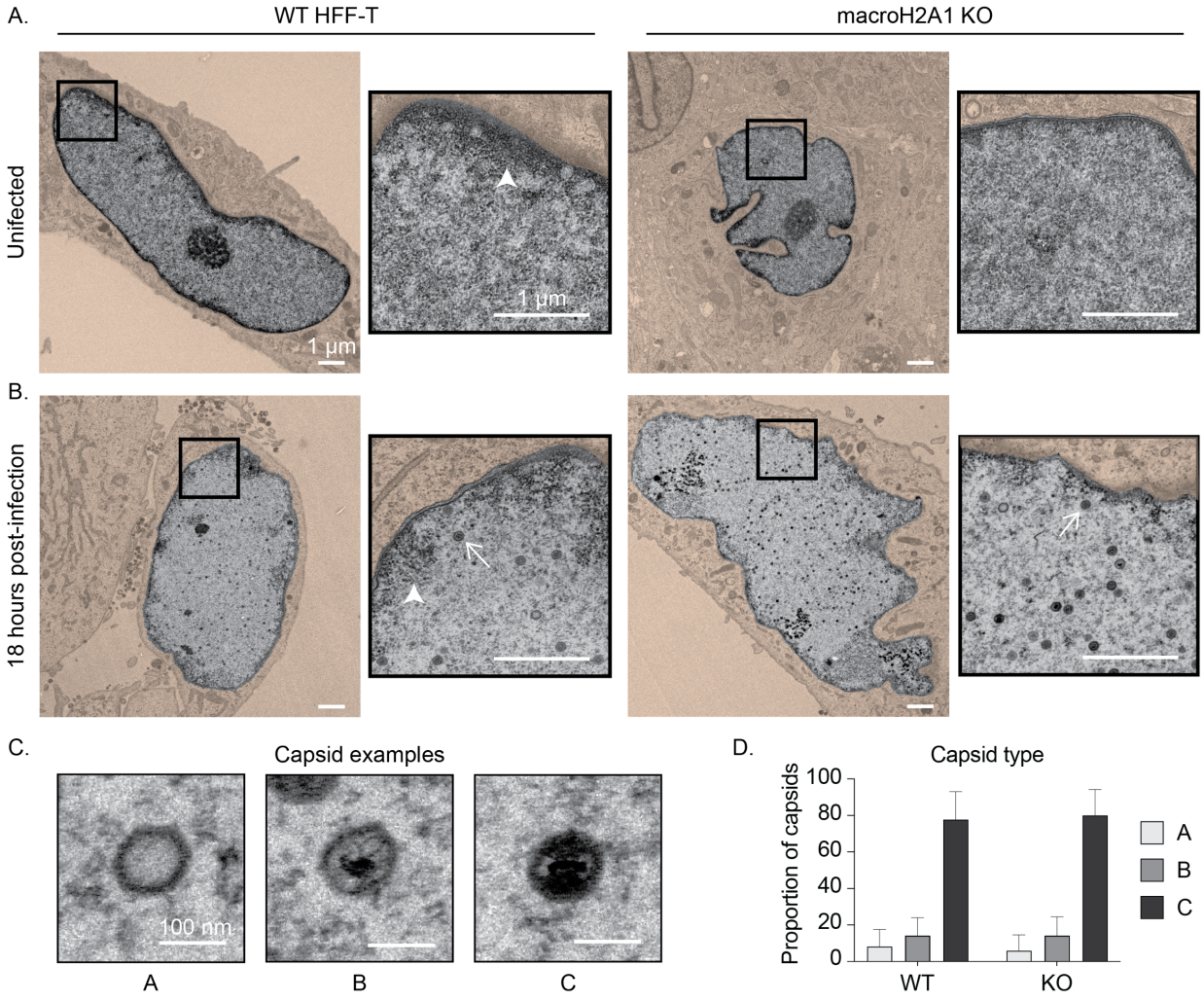

Supplemental Figure S3. HSV-1 capsid formation is independent of macroH2A1.

A. Transmission electron microscopy (TEM) images of representative nuclei of uninfected WT (left) or macroH2A1 KO (right) HFF-Ts. Regions outside of the nucleus are colorized orange. Insets show enlarged views of respective boxed areas containing peripheral heterochromatin. Arrowhead indicates high density heterochromatin.

B. TEM images of representative WT and macroH2A1 knockout nuclei at 18 hours post-infection with HSV-1. Insets show enlarged views of respective boxed areas containing capsids within nuclei. Arrowhead indicates heterochromatin, arrow indicates viral capsid.

C. TEM images of representative A (empty), B (scaffolding proteins, but no genome), and C (full) HSV-1 capsids. Scale bars as noted for all TEM images.

586 D. Quantification of capsid types within nuclei from B. Values for each capsid type are
587 shown as a proportion of total capsids.
588

589 **MATERIALS AND METHODS**

590 **Cells and viruses:**

591 Primary human foreskin fibroblasts (HFFs), hTERT-immortalized HFFs, hTERT-immortalized
592 macroH2A1 knockout HFFs were cultured using standard methods with 10% FBS and 1%
593 penicillin-streptomycin as previously described (*49*). Cells were grown at 37 °C with 5% CO_2
594 and tested for mycoplasma contamination approximately once a month.

595 The lab adapted strain of HSV-1, *syn 17+* (*50*) was used for all experiments unless otherwise
596 noted. Monolayers of cells were infected for 1 hour at 37 °C as previously described (*51*). An
597 MOI of 3 was used for all experiments, except for EM samples which used MOI of 10. Cells
598 were collected at mock, 4-, 8-, 12- hpi for western blot. Supernatant was collected at 8- and 12-
599 hpi for plaque assays. Virus stock was grown by infecting Vero cells at an MOI of 0.0001. Virus
600 was harvested ~60-80 hours post-infection and titered on U2OS cells to determine stock plaque
601 forming units per mL (PFU/mL). Experimental plaque assays were set up in Vero cells. Plaque
602 assays were set up on serial 10-fold dilutions in serum-free DMEM. Virus was left on cells for 1
603 hour then aspirated. Cells were washed with 1X PBS (pH 7.46) and 2% methylcellulose overlay
604 in DMEM with 2% FBS and 0.5% penicillin-streptomycin was added to wells. Plaques were fixed
605 with 0.2% crystal violet between 96-100 hours post infection and plaques were counted by
606 hand. All plaque assays were set up with 2 technical replicates.

607 Clinical isolates were acquired in 1994 and 1995 from oral swab collections. Samples were de-
608 identified on collection. Patients provided daily home collections of oral swabs, and qPCR was
609 used to detect how many days HSV was detected in these swabs. Patients that had detectable
610 HSV in only a few swabs were classified as “low-shedders” and patients that had a high
611 percentage of days with positive swabs were classified as “high-shedders.” Stocks were a gift
612 from the lab of Keith Jerome.

613 Table 1: Cell line sources.

Cell Line	Source
Human: RPE-1 (hTERT-immortalized)	Gift of E. Hatch Lab (*52*) (Invitrogen)
Human: Primary HFF	Gift of D. Galloway Lab
Human: HFF (hTERT-immortalized)	Gift of J. Kamil Lab (*53*)

African Green Monkey: Vero	Gift of A. Geballe Lab (*54*)

614

615 **Knockout of macroH2A1:**

616 MacroH2A1 guide RNA (gRNA, see Table 3) was cloned into TLCv2 (Addgene plasmid: 87360),
617 a plasmid encoding doxycycline-inducible Cas9-2A-GFP and gRNA expression. To generate
618 lentiviral particles, $1.0x10^7$ HEK293T cells were transfected with 12 µg TLCV2_sg_mH2A1, 8 µg
619 pMDL (Addgene plasmid: 12251), 4 µg VSVg, and 2.5 µg pREV (Addgene plasmid: 115989)
620 using Attractene transfection reagent (Qiagen: 301005). Lentivirus was harvested at 24-, 48-,
621 and 72-hours post-transfection, filtered through 0.2 µm filters, aliquoted, flash frozen with liquid
622 nitrogen, and stored at -80C. 2 mL of thawed filtered lentivirus was used to transduce
623 approximately $2.25x10^6$ HFF-T or $3x10^6$ RPE cells in 10 cm plates with 8 µg/mL polybrene
624 (Millipore-Sigma: TR-1003-G). Cells were allowed to reach confluence before selection with 1
625 µg/mL puromycin for 3 days. Cells were then sorted by GFP positivity or counted by
626 hemocytometer, plated at 1 cell per well into 96-well plates, and selected through serial
627 expansion of colonies. Selected cells were screened for macroH2A1 knockout by western blot.

628 **Infections with Tazemetostat pretreatment:**

629 HFFs and macroH2A1 KO HFFs were treated with DMSO or 10 µM of Tazemetostat (Taz)
630 (MedChem: HY-13803) in DMSO for 3 days prior to infection. Cells were then infected at MOI of
631 3 and after 1 hour of incubation with virus, fresh media with 10µM Taz was added to previously
632 treated cells. Control samples were treated with equivalent volumes of DMSO. Samples were
633 harvested as above.

634 **Western Blotting:**

635 Western blotting was performed as previously described (*49*). Briefly, cells were counted,
636 pelleted, resuspended in 1x NuPAGE lithium dodecyl sulfate (LDS) sample buffer (Fisher
637 Scientific: NP007) + 5% 2-betamercaptoethanol, and boiled for 15 minutes. Protein lysates were
638 separated by 13.5% SDS-PAGE gels using NuPAGE MOPS buffer (Fisher Scientific: NP0001)
639 at 75 volts for 30 minutes then 110 volts for 100 minutes, then transferred to a nitrocellulose
640 membrane (Bio-Rad) at 100 volts for 70 minutes using Transfer Buffer (25 mM Tris Base, 100
641 mM glycine, 20% methanol). Membranes were ponceau stained and imaged. Membranes were
642 blocked in 5% milk in Tris-buffered saline with Tween (TBST) for 1 hour, then probed with
643 primary antibody overnight (see Table 2). Membranes were washed with TBST for thirty
644 minutes, incubated with secondary antibodies conjugated to horseradish peroxidase (α-mouse
645 or α-rabbit; 1:5000) at room temperature for 1 hour, washed with TBST for thirty minutes, and

646 detected using Clarity Western ECL Substrate (Bio-Rad: 1705061) and Chemidoc MP Imaging
647 System (Bio-Rad). Images were formatted using Adobe Photoshop and Illustrator.

648 Table 2: Sources and identification of antibodies used.

Antibody	Source	Identifier	Use (Concentration)
Mouse anti-actin	Abcam	Cat: 5441	WB (1:10,000)
Mouse anti-gH	Abcam	Cat: 110227	WB (1:1,000)
Rabbit anti-H3	Abcam	Cat: 1791	WB (1:20,000)
Rabbit anti-H3K27me3	Cell Signal Technologies	Cat: 9733T	WB/CUT&Tag (1:100)
Rabbit anti-H3K9me3	Abcam	Cat: 8898	WB (1:1,000)
Rabbit anti-H4	Abcam	Cat: 10158	WB (1:1,000)
Mouse anti-ICP0	Santa Cruz Biotechnology	Cat: 53070	WB (1:1,000)
Rabbit anti-macroH2A1	Abcam	Cat: 37264	WB (1:1,000) CUT&Tag (1:100)
Rabbit anti-macroH2A1.1	Cell Signaling Technology	Cat: 12455S	WB (1:1,000)
Mouse anti-macroH2A1.2	Cell Signaling Technology	Cat: 4827S	WB (1:1,000)
Rabbit anti-macroH2A2	Active Motif	Cat: 39874	WB (1:1,000)
HRP-conjugated anti-VP16	Santa Cruz Biotechnology	Cat. 7546	WB (1:1,000)
Peroxidase-AffiniPure Goat Anti-Mouse	Jackson Immunoresearch Laboratories	Cat: 115-035-003	WB (1:5,000)
Peroxidase-AffiniPure Goat Anti-Rabbit	Jackson Immunoresearch Laboratories	Cat: 111-035-045	WB (1:5,000)
Rabbit anti-mouse IgG	Abcam	Cat: 46540	CUT&Tag (1:100)
Guinea pig anti-rabbit IgG	Antibodies Online	Cat: AB1N101961	CUT&Tag (1:100)

649

650 **Quantification of HSV-1 genomes by ddPCR:**

651 Cells were harvested at the indicated times post-infection by trypsinization, washed with 1X
652 PBS and centrifuged at 5000 xg for 2 minutes. Pellets were flash-frozen in liquid nitrogen and
653 stored at -80 °C until processed. HSV-1 DNA within cells was isolated from frozen pellets using
654 QIAamp DNAMini Kit (Qiagen: 51304).

655 Supernatants were harvested at the indicated times post-infection, centrifuged at > 3500 xg and
656 filtered through 40 micron sterile syringe filters. DNA on the exterior of filtered capsids was
657 digested for 1 hour at 25 °C with 20.3 units DNase (Qiagen: 79254) supplemented with 10 mM
658 $MgCl_2$. DNase was inactivated at 75 °C for 10 minutes followed by vortexing. Capsids were
659 digested with 3 mg/mL proteinase K (Fisher Scientific: BP1700) in 100 mM KCl, 25 mM EDTA,
660 10 mM Tris-HCl pH 7.4 and 1% Igepal for 1 hour at 50 °C. HSV-1 genomes from digested
661 capsids were isolated using QIAamp DNAMini Kit.

662 A duplexed digital droplet PCR was performed to measure the levels of cellular or supernatant
663 HSV-1 genomes on the QX100 droplet digital PCR system (Bio-Rad Laboratories, Hercules,
664 CA) using a primer/probe set specific to HSV-1 gB. Cell numbers were determined using a
665 primer/probe set specific to human Beta-globin, a reference gene that exists at two copies per
666 cell. See Table 3 for oligonucleotide sequences, as have been previously established for HSV-1
667 (*55*). The digital droplet PCR (ddPCR) reaction mixture consisted of 12.5 µL of a 2X ddPCR
668 Supermix for Probes no dUTP (Bio-Rad: 1863024), 1.25 µL of each 20X primer-probe mix, and
669 10 µL of template DNA. 20 µL of each reaction mixture was loaded onto a disposable plastic
670 cartridge (Bio-Rad: 1864008) with 70 µL of droplet generation oil (Bio-Rad: 1863005) and
671 placed in the droplet generator (Bio-Rad). Droplets generated were transferred to a 96-well PCR
672 plate (Bio-Rad 12001925), and PCR amplification was performed on a Bio-Rad C1000 Touch
673 Thermal Cycler with the following conditions: 95 °C for 10 minutes, 40 cycles of 94 °C for 30
674 seconds, and 60 °C for 1 minute, followed by 98 °C for 10 minutes and ending at 4 °C. After
675 amplification, the plate was loaded onto the droplet reader (Bio-Rad: QX200), and the droplets
676 from each well of the plate were automatically read with droplet reader oil (Bio-Rad: 186-3004)
677 at a rate of 32 wells per hour. Data were analyzed with QuantaSoft analysis software and
678 quantitation of target molecules presented as copies per µL of PCR reaction. HSV-1 genome
679 values were standardized to cellular β-globin levels. Experiments were completed in biological
680 triplicate and statistical analysis was performed using Prism v10 (GraphPad Software).

681 Table 3: Primers used for knockout and ddPCR

CRISPR MacroH2A1 gRNA	CCTCAATAGCAAGCCATCCTGT
HSV1_gB_qPCR_F1	CCGTCAGCACCTTCATCGA
HSV1_gB_qPCR_R1	CGCTGGACCTCCGTGTAGTC
HSV1_gB_probe1	6FAM-CCACGAGATCAAGGACAGCGGCC-BHQ1
beta-globin_qPCR_F1	TGAAGGCTCATGGCAAGAAA
beta-globin_qPCR_R1	GCTCACTCAGTGTGGCAAAGG
beta-globin_probe2_hex	/5HEX/TC CAG GTG AGC CAG GCC ATC ACT A/3BHQ_1/

682 **Cleavage Under Targets & Tagmentation (CUT&Tag):**

683 Two biological replicates per time point were obtained from independent infections. Protocol
684 was adapted from the established CUT&Tag methods (*56*). Cells were harvested using trypsin,
685 washed three times with ice-cold phosphate-buffered saline (PBS) via centrifugation at 600 xg
686 for 3 minutes and counted using a hemocytometer. Nuclei from 600,000 cells were isolated by
687 hypotonic lysis in 1 mL buffer NE1 (20 mM HEPES-KOH pH 7.9; 10 mM KCl; 0.5 mM
688 spermidine; 0.1% Triton X-100; 20% Glycerol; Roche EDTA-free protease inhibitor) for 10
689 minutes on ice followed by centrifugation at 1300 xg for 4 minutes. Nuclei were resuspended in
690 Wash buffer (20 mM HEPES-NaOH pH 7.5; 150 mM NaCl; 0.5 mM spermidine; Roche EDTA-
691 free protease inhibitor) and counted using a hemocytometer. BioMag Plus Concanavalin A
692 coated beads (Polysciences: 86057-3) were equilibrated with Binding buffer (20 mM HEPES-
693 KOH pH 7.9; 10 mM KCL; 1mM $CaCl_2$; 1 mM $MnCl_2$). Beads (5 µL) were mixed with aliquots of
694 75,000 nuclei and incubated at 25 °C for 10 minutes followed by magnetic separation of beads.
695 Beads were resuspended in 50 µL primary antibody [anti-mH2A1 (Abcam: ab37624), anti-
696 H3K27me3 (Cell Signaling:9733) or anti-mouse IgG (Abcam: ab46540) in Wash buffer
697 supplemented with 2 mM EDTA and 0.1% bovine serum albumin (BSA) and incubated on a
698 nutator at 4 °C overnight. The beads were decanted on a magnet stand then resuspended in 50
699 µL secondary antibody [Guinea pig anti-rabbit IgG (Antibodies-Online: ABIN101961) 1:100] in
700 Wash buffer supplemented with 2 mM EDTA and 0.1% BSA and incubated on a nutator at room
701 temperature for 1 hour. The beads were decanted on a magnet stand and washed with 200 µL
702 Wash buffer, then were resuspended in 50 µL pA-Tn5 (1:200) in 300-Wash buffer (Wash buffer
703 containing 300 mM NaCl) and incubated on a nutator at room temperature for 1 hour. The
704 beads were washed twice with 200 µL 300-Wash buffer, then resuspended in 50 µL
705 Tagmentation buffer (300-Wash buffer supplemented with 10 mM $MgCl_2$) and incubated at 37
706 °C for 1 hour. Beads were then washed with 50 µL TAPS wash buffer (10 mM TAPS pH 8.5, 0.2
707 mM EDTA), then resuspended in 5 µL TAPS wash buffer supplemented with 0.1% SDS and
708 incubated at 58 °C for 1 hour. SDS was neutralized on ice with 15 µL 0.67% Triton-X100. 2 µL
709 of 10 mM indexed P5 and P7 primer solutions and 25 µL NEBnext High-Fidelity 2X Master Mix
710 (New England BioLabs: ME541L) were added. Gap-filling and 15 cycles of PCR were performed
711 using an MJ PTC-200 Thermocycler. Library clean-up was performed by incubating beads with
712 65 µL SPRI bead slurry for 5-10 minutes, then magnetization and two washes with 200 µL 80%
713 ethanol. Libraries were eluted with 22 µL Tris-HCl pH 8.0 and 2 µL was used for Agilent 4200
714 Tapestation analysis. The barcoded libraries were mixed to achieve equimolar representation as

715 desired aiming for a final concentration as recommended by the manufacturer for sequencing
716 on an Illumina HiSeq 2500 2-lane Turbo flow cell.

717 **CUT&Tag data processing:**

718 CUT&Tag raw sequencing data were aligned to a custom genome made by concatenating
719 human (hg38), HSV (JN555585.1), and E. coli (U00096.3 Escherichia coli str. K-12 substr.
720 MG1655, complete genome). We performed alignments using bowtie2.

721 **Domain calling:**

722 Coverage at 100 bp windows of the human hg38 reference genome was calculated as number
723 of reads of given length (120-1000 bp for the analyses presented here) that mapped at that
724 window normalized by the factor N:

725 N= 10,000/(Total number of reads that mapped to E. coli genome)

726 Here 10,000 is an arbitrarily chosen number. The normalized coverage at each base-pair from
727 each replicate was averaged when combining multiple replicates. The normalized read density
728 in 100 bp bins were then smoothed with a running average over the bins spanning +/- 1000 bp
729 around each bin. We then calculated the genome-wide distribution of normalized read density
730 and medians that were plotted in Figure S1. We averaged medians across WT macroH2A1
731 datasets (mock, 4hpi, 8hpi, and 12hpi), and multiplied the average by 2, to set the cutoff for
732 domain definition for macroH2A1 datasets. We defined a similar cutoff for H3K27me3 datasets
733 using H3K27me3 WT datasets.

734 **Identifying domain level dynamics of macroH2A1 over time course of infection:**

735 To measure changes in macroH2A1 across time points where the domain boundaries are not
736 the same, we first concatenated domain definitions from all macroH2A1 datasets and then
737 defined a set of non-overlapping intervals using the “disjoin” method of GenomicRanges R
738 package (*57*). We then calculated the log2 ratio of macroH2A1 enrichment over IgG for the non-
739 overlapping regions for the mock, 4, 8, and 12hpi. The 4, 8, and 12hpi enrichments were then
740 divided by the enrichment of the mock dataset to obtain change in macroH2A1 over time course
741 at the non-overlapping regions. k-means clustering (k=6) using R (*58*) was performed on the
742 matrix where the rows are the non-overlapping regions and the columns are change in
743 macroH2A1 over mock at 4, 8, and 12hpi. We extended the non-overlapping regions by 5 bp on
744 each end and then merged regions within each cluster using “reduce” method of
745 GenomicRanges, to obtain domains in each cluster. We recalculated change in macroH2A1 at
746 4, 8, and 12hpi over mock, which was used to plot heatmaps and boxplots shown in Figure 1

747 and Figure S1. H3K27me3 enrichment for WT and macroH2A1 KO cells was calculated at
748 clustered macroH2A1 domains.

749 **RNA sequencing:**

750 Three biological replicates per time point were obtained from independent infections. Cells were
751 harvested at the indicated times post-infection by trypsinization, washed with PBS and
752 centrifuged at 5000 xg for 2 minutes. Pellets were lysed with TRIzol (Thermo Fisher: 15-596-
753 026) and total RNA was harvested according to manufacturer's instructions. RNAs were then
754 treated with DNase (Qiagen: 79254) on RNeasy columns (Qiagen: 74104) per manufacturer's
755 instructions. RNA was precipitated with 3 volumes ice-cold 96% ethanol, 1 volume 3 M sodium
756 acetate pH 5.5, and 1 µL glycogen (Thermo Fischer: R055) overnight at -80 °C. Precipitated
757 RNAs were pelleted at 15,000 xg and 4 °C for 30 minutes, washed with ice-cold 75% ethanol
758 and spun as above for 10 min. RNA was resuspended in nuclease-free water.

759 RNA was quantified by Nanodrop and integrity analyzed with the 4200 Tapestation Bioanalyzer
760 system (Agilent). 500 ng of total RNA with an RNA Integrity Number (RIN) greater than 9.5 were
761 used to prepare sequencing libraries with the TruSeq® Stranded mRNA Library Prep Kit
762 (Illumina: 20020594). Library concentrations were measured with Qubit dsDNA HS Assay Kit
763 (Thermo Fisher: Q32854) then analyzed with Agilent High Sensitivity D5000 ScreenTape
764 System and pooled. Libraries were sequenced with 100-bp paired-end reads on an Illumina
765 NovaSeq 6000 SP sequencer at the Fred Hutch Genomics Core Facility

766 **RNA/4sU-RNA/Hi-C data processing:**

767 Fastq files were filtered to exclude reads that didn't pass Illumina's base call quality threshold.
768 STAR v2.7.1 (*59*) with 2-pass mapping was used to align paired-end reads to a combined
769 reference of human genome build hg38 and HSV1 genome JN555585.1
770 (https://www.ncbi.nlm.nih.gov/nuccore/JN555585.1/). FastQC 0.11.9
771 (https://www.bioinformatics.babraham.ac.uk/projects/fastqc/) and RSeQC 4.0.0 (*60*) were used
772 for QC including insert fragment size, read quality, read duplication rates, gene body coverage
773 and read distribution in different genomic regions. FeatureCounts (*61*) in Subread 1.6.5 was
774 used to quantify gene-level expression by strand-specific paired-end read counting.

775 Gene annotation were based on GENCODE V31 (https://www.gencodegenes.org/human/) and
776 GCA_000859985.2_ViralProj15217 (https://www.ncbi.nlm.nih.gov/data-
777 hub/genome/GCF_000859985.2/). For HSV1, annotated genes were collapsed into non-
778 overlapping transcribed regions, e.g. X indicating a transcribed region unique to gene X, X:Y
779 indicating an overlapping transcribed region for genes X and Y, and so on.

780 Bioconductor package edgeR 3.26.8 (*62*) was used to detect differential gene expression
781 between sample groups. Genes with low expression were excluded by requiring at least one
782 count per million in at least N samples (N is equal to the number of samples in the smaller
783 group). The filtered expression matrix was normalized by TMM method
784 (https://genomebiology.biomedcentral.com/articles/10.1186/gb-2010-11-3-r25) and subject to
785 significance testing using quasi-likelihood pipeline implemented in edgeR. Genes were deemed
786 differentially expressed if fold changes were greater than 2 in either direction and Benjamini-
787 Hochberg adjusted p-values were less than 0.01.

788 The intervals representing start and end of each gene were intersected with clustered
789 macroH2A1 domains to obtain cluster assignments for genes. Intersection was performed using
790 "intersect" function of bedtools (*63*). Genes that did not uniquely intersect with domains in a
791 single cluster were discarded. The cluster assignments for genes were used for plotting total
792 RNA fold changes in Figure 2. Reads per kilobase of transcript per million reads mapped
793 (RPKM) values for 4sU-RNA was obtained from GEO (GSE59717) and converted to transcripts
794 per million (TPM). The TPM values across two 4sU-RNA replicates for each condition was
795 averaged and box plots were generated similarly to total RNA.

796 For calculating eigenvector distributions, compartment wig file was downloaded from the
797 following link:

798 https://4dn-open-data-public.s3.amazonaws.com/fourfront-webprod/wfoutput/b543cbf4-ce54-
799 4d2d-8960-281528ff18a6/4DNFI342UZP1.bw

800 Regions from compartment file intersecting with each domain cluster were extracted and the
801 values were used for generating box plots shown in Figure 2D.

802 **Electron Microscopy:**

803 Cells were fixed in 2% paraformaldehyde and 2.5% glutaraldehyde in 0.1M sodium cacodylate
804 buffer (pH 7.3) at 4 °C. Fixed cells were rinsed briefly in 1% sucrose in 50mM cacodylate (pH
805 7.2), then postfixed on ice for 30 mins in a solution of 1% osmium (EM Sciences: RT19152) and
806 0.8% potassium ferricyanide in 50mM cacodylate (pH 7.2). Cell pellets were washed twice
807 briefly at 25 °C in 1% sucrose in 50mM cacodylate (pH 7.2), then washed in three changes of
808 50mM cacodylate (pH 7.2) for 5 min each. Cell pellets were treated with 0.2% tannic acid
809 (Sigma-Aldrich: 1401-55-4) in 50 mM cacodylate (pH 7.2) for 15 minutes at 25 °C, then rinsed
810 several times in water. Cells were dehydrated through a graded ethanol series and embedded
811 in Epon 12 resin (Ted Pella: 18010). 70nm thin sections were cut using an Ultracut UC7
812 ultramicrotome (Leica Mikrosysteme) and collected on 200 mesh formvar/carbon copper grids

813 (Ted Pella: 01800). Sections were stained with 2% aqueous uranyl acetate and Reynolds lead
814 citrate. Cell pellet sections were imaged using a Talos L120C microscope operated at 120kV
815 with a Ceta-16M (4096 x 4096) camera (ThermoFisher Scientific).

816 All data were collected at spot size 5 with a 100um C2 aperture and 70um objective aperture.
817 For quantification, nuclei were targeted at 1250x and manually circled. Autofocus was set to -
818 2.0um. Nuclei were then imaged at 11000x as a montage and stitched together automatically
819 using SerialEM (Nexperion Inc). Stitched maps were exported as uncompressed 16-bit tif files
820 for further analysis. For qualitative analysis, images were manually focused to -2.0um defocus
821 and then 20 1-second frames were collected and drift-corrected using Velox software (Thermo
822 Fisher Scientific, Eindhoven, NL). Final summed images were exported as 16-bit tif files and
823 cropped using ImageJ.

824 Image analysis pipelines for counting capsids and for measuring chromatin density at the
825 nuclear envelope were deployed in MATLAB R2020b. Scripts are available on the Fred Hutch
826 GitHub repository. Capsid pipeline follows three steps: 1- nuclear boundaries identification, 2-
827 capsid detection, 3- capsid classification. Nuclear boundaries were identified with user input, by
828 outlining a freehand contour of the nucleus of interest, from which a binary mask is extracted.
829 Capsid detection was performed on the median-filtered complement of the original image, using
830 a Circular Hough Transform based algorithm, with phase coding for radii estimation (*64*), and
831 search radius ranging from 10.6 to 31.7 nm. Capsids residing within the nuclear mask were then
832 counted and classified. Detected capsids were classified in three categories (Empty,
833 Intermediate and Full), depending on the distribution of the pixel grayscale intensities within the
834 capsids relative to a normal distribution.

835 Width of heterochromatin abutting the nuclear envelope was quantified by measuring the length
836 of the binarized chromatin from 1D intensity profiles along the normal of the nuclear perimeter,
837 sampled at every 10 perimeter pixels. Dense heterochromatin was binarized using global Otsu's
838 thresholding method applied to the background-corrected complement of the contrast-adjusted
839 original image. Noise from the binarized image was further reduced by applying a 2D order
840 statistic filter using the minimum value of a varying domain interactively defined by the user, with
841 default value of 8-by-8 pixels. The resulting heterochromatin density distribution was normalized
842 to the total length of the nucleus' perimeter.

843

844

845 **REFERENCES CITED**

846

847 1. D. M. Knipe, A. Cliffe, Chromatin control of herpes simplex virus lytic and latent infection. *Nat Rev*
848 *Microbiol*. 6, 211–221 (2008).

849 2. K. Monier, J. C. G. Armas, S. Etteldorf, P. Ghazal, K. F. Sullivan, Annexation of the interchromosomal
850 space during viral infection. *Nat Cell Biol*. 2, 661–665 (2000).

851 3. K. Kulej, D. C. Avgousti, S. Sidoli, C. Herrmann, A. N. D. Fera, E. T. Kim, B. A. Garcia, M. D.
852 Weitzman, Time-resolved Global and Chromatin Proteomics during Herpes Simplex Virus Type 1 (HSV-
853 1) Infection. *Mol Cell Proteomics*. 16, S92–S107 (2017).

854 4. V. Aho, E. Mäntylä, A. Ekman, S. Hakanen, S. Mattola, J.-H. Chen, V. Weinhardt, V. Ruokolainen, B.
855 Sodeik, C. Larabell, M. Vihinen-Ranta, Quantitative Microscopy Reveals Stepwise Alteration of
856 Chromatin Structure during Herpesvirus Infection. *Viruses*. 11, 935 (2019).

857 5. V. Aho, S. Salminen, S. Mattola, A. Gupta, F. Flomm, B. Sodeik, J. B. Bosse, M. Vihinen-Ranta,
858 Infection-induced chromatin modifications facilitate translocation of herpes simplex virus capsids to the
859 inner nuclear membrane. *Plos Pathog*. 17, e1010132 (2021).

860 6. M. Myllys, V. Ruokolainen, V. Aho, E. A. Smith, S. Hakanen, P. Peri, A. Salvetti, J. Timonen, V.
861 Hukkanen, C. A. Larabell, M. Vihinen-Ranta, Herpes simplex virus 1 induces egress channels through
862 marginalized host chromatin. *Sci Rep-uk*. 6, 28844 (2016).

863 7. P. Chi, C. D. Allis, G. G. Wang, Covalent histone modifications — miswritten, misinterpreted and mis-
864 erased in human cancers. *Nat Rev Cancer*. 10, 457–469 (2010).

865 8. R. Margueron, D. Reinberg, The Polycomb complex PRC2 and its mark in life. *Nature*. 469, 343–349
866 (2011).

867 9. V. Pasque, A. Gillich, N. Garrett, J. B. Gurdon, Histone variant macroH2A confers resistance to
868 nuclear reprogramming. *Embo J*. 30, 2373–2387 (2011).

869 10. F. G. Ghiraldini, D. Filipescu, E. Bernstein, Solid tumours hijack the histone variant network. *Nat Rev*
870 *Cancer*. 21, 257–275 (2021).

871 11. M. J. Gamble, W. L. Kraus, Multiple facets of the unique histone variant macroH2A: From genomics
872 to cell biology. *Cell Cycle*. 9, 2568–2574 (2010).

873 12. G. Timinszky, S. Till, P. O. Hassa, M. Hothorn, G. Kustatscher, B. Nijmeijer, J. Colombelli, M.
874 Altmeyer, E. H. K. Stelzer, K. Scheffzek, M. O. Hottiger, A. G. Ladurner, A macrodomain-containing
875 histone rearranges chromatin upon sensing PARP1 activation. *Nat Struct Mol Biol*. 16, 923–929 (2009).

876 13. H. Chen, P. D. Ruiz, L. Novikov, A. D. Casill, J. W. Park, M. J. Gamble, MacroH2A1.1 and PARP-1
877 cooperate to regulate transcription by promoting CBP-mediated H2B acetylation. *Nat Struct Mol Biol*. 21,
878 981–989 (2014).

879 14. A. Kapoor, M. S. Goldberg, L. K. Cumberland, K. Ratnakumar, M. F. Segura, P. O. Emanuel, S.
880 Menendez, C. Vardabasso, G. LeRoy, C. I. Vidal, D. Polsky, I. Osman, B. A. Garcia, E. Hernando, E.
881 Bernstein, The histone variant macroH2A suppresses melanoma progression through regulation of CDK8.
882 *Nature*. 468, 1105–1109 (2010).

883 15. J. Douet, D. Corujo, R. Malinverni, J. Renauld, V. Sansoni, M. P. Marjanović, N. Cantariño, V.
884 Valero, F. Mongelard, P. Bouvet, A. Imhof, M. Thiry, M. Buschbeck, MacroH2A histone variants
885 maintain nuclear organization and heterochromatin architecture. *J Cell Sci*. 130, 1570–1582 (2017).

886 16. Y. Fu, P. Lv, G. Yan, H. Fan, L. Cheng, F. Zhang, Y. Dang, H. Wu, B. Wen, MacroH2A1 associates
887 with nuclear lamina and maintains chromatin architecture in mouse liver cells. *Sci Rep-uk*. 5, 17186
888 (2015).

889 17. C. James, M. Harfouche, N. J. Welton, K. M. Turner, L. J. Abu-Raddad, S. L. Gottlieb, K. J. Looker,
890 Herpes simplex virus: global infection prevalence and incidence estimates, 2016. *B World Health Organ*.
891 98, 315–329 (2020).

892 18. K. J. Looker, A. S. Magaret, M. T. May, K. M. E. Turner, P. Vickerman, L. M. Newman, S. L.
893 Gottlieb, First estimates of the global and regional incidence of neonatal herpes infection. *Lancet Global*
894 *Heal*. 5, e300–e309 (2017).

895 19. L. A. Sadowski, R. Upadhyay, Z. W. Greeley, B. J. Margulies, Current Drugs to Treat Infections with
896 Herpes Simplex Viruses-1 and -2. *Viruses*. 13, 1228 (2021).

897 20. J. Matthias, S. du Bernard, J. A. Schillinger, J. Hong, V. Pearson, T. A. Peterman, Estimating neonatal
898 herpes simplex virus incidence and mortality using capture-recapture, Florida. *Clin Infect Dis*. 73,
899 ciaa727- (2020).

900 21. A. Berkhout, V. Kapoor, C. Heney, C. A. Jones, J. E. Clark, V. L. Vaska, M. Lai, C. Nourse, Herpes
901 Simplex Virus Infection in Infants: 13 Year Evaluation (2005–2017) of Laboratory Confirmed Cases in
902 Queensland, Australia. *Pediatr Infect Dis J*. Publish Ahead of Print (2020),
903 doi:10.1097/inf.0000000000002970.

904 22. P. G. Spear, Herpes simplex virus: receptors and ligands for cell entry. *Cell Microbiol*. 6, 401–410
905 (2004).

906 23. V. Tiwari, M. Oh, M. Kovacs, S. Y. Shukla, T. Valyi-Nagy, D. Shukla, Role for nectin-1 in herpes
907 simplex virus 1 entry and spread in human retinal pigment epithelial cells. *Febs J*. 275, 5272–5285
908 (2008).

909 24. R. B. Deal, J. G. Henikoff, S. Henikoff, Genome-Wide Kinetics of Nucleosome Turnover Determined
910 by Metabolic Labeling of Histones. *Science*. 328, 1161–1164 (2010).

911 25. E. M. Riising, I. Comet, B. Leblanc, X. Wu, J. V. Johansen, K. Helin, Gene Silencing Triggers
912 Polycomb Repressive Complex 2 Recruitment to CpG Islands Genome Wide. *Mol Cell*. 55, 347–360
913 (2014).

914 26. E. Lieberman-Aiden, N. L. van Berkum, L. Williams, M. Imakaev, T. Ragoczy, A. Telling, I. Amit,
915 B. R. Lajoie, P. J. Sabo, M. O. Dorschner, R. Sandstrom, B. Bernstein, M. A. Bender, M. Groudine, A.

916 Gnirke, J. Stamatoyannopoulos, L. A. Mirny, E. S. Lander, J. Dekker, Comprehensive Mapping of Long-
917 Range Interactions Reveals Folding Principles of the Human Genome. *Science*. 326, 289–293 (2009).

918 27. S. S. P. Rao, M. H. Huntley, N. C. Durand, E. K. Stamenova, I. D. Bochkov, J. T. Robinson, A. L.
919 Sanborn, I. Machol, A. D. Omer, E. S. Lander, E. L. Aiden, A 3D Map of the Human Genome at
920 Kilobase Resolution Reveals Principles of Chromatin Looping. *Cell*. 159, 1665–1680 (2014).

921 28. W. Cai, P. A. Schaffer, Herpes simplex virus type 1 ICP0 regulates expression of immediate-early,
922 early, and late genes in productively infected cells. *J Virol*. 66, 2904–2915 (1992).

923 29. R. Naldinho-Souto, H. Browne, T. Minson, Herpes Simplex Virus Tegument Protein VP16 Is a
924 Component of Primary Enveloped Virions. *J Virol*. 80, 2582–2584 (2006).

925 30. E. U. Lorentzen, B. R. Eing, W. Hafezi, R. Manservigi, J. E. Kühn, Replication-Competent Herpes
926 simplex Virus Type 1 Mutant Expressing an Autofluorescent Glycoprotein H Fusion Protein.
927 *Intervirology*. 44, 232–242 (2001).

928 31. R. Rickels, D. Hu, C. K. Collings, A. R. Woodfin, A. Piunti, M. Mohan, H.-M. Herz, E. Kvon, A.
929 Shilatifard, An Evolutionary Conserved Epigenetic Mark of Polycomb Response Elements Implemented
930 by Trx/MLL/COMPASS. *Mol Cell*. 63, 318–328 (2016).

931 32. J. K. Lue, J. E. Amengual, Emerging EZH2 Inhibitors and Their Application in Lymphoma. *Curr*
932 *Hematol Malig R*. 13, 369–382 (2018).

933 33. J. H. Arbuckle, P. J. Gardina, D. N. Gordon, H. D. Hickman, J. W. Yewdell, T. C. Pierson, T. G.
934 Myers, T. M. Kristie, Inhibitors of the Histone Methyltransferases EZH2/1 Induce a Potent Antiviral State
935 and Suppress Infection by Diverse Viral Pathogens. *Mbio*. 8, e01141-17 (2017).

936 34. V. Aho, M. Myllys, V. Ruokolainen, S. Hakanen, E. Mäntylä, J. Virtanen, V. Hukkanen, T. Kühn, J.
937 Timonen, K. Mattila, C. A. Larabell, M. Vihinen-Ranta, Chromatin organization regulates viral egress
938 dynamics. *Sci Rep-uk*. 7, 3692 (2017).

939 35. W. Gibson, B. Roizman, Proteins Specified by Herpes Simplex Virus VIII. Characterization and
940 Composition of Multiple Capsid Forms of Subtypes 1 and 2. *J Virol*. 10, 1044–1052 (1972).

941 36. X.-K. Yu, C. M. O'Connor, I. Atanasov, B. Damania, D. H. Kedes, Z. H. Zhou, Three-Dimensional
942 Structures of the A, B, and CCapsids of Rhesus Monkey Rhadinovirus: Insights into
943 GammaherpesvirusCapsid Assembly, Maturation, and DNAPackaging. *J Virol*. 77, 13182–13193 (2003).

944 37. T. Hennig, M. Michalski, A. J. Rutkowski, L. Djakovic, A. W. Whisnant, M.-S. Friedl, B. A. Jha, M.
945 A. P. Baptista, A. L'Hernault, F. Erhard, L. Dölken, C. C. Friedel, HSV-1-induced disruption of
946 transcription termination resembles a cellular stress response but selectively increases chromatin
947 accessibility downstream of genes. *Plos Pathog*. 14, e1006954 (2018).

948 38. Y. Cai, Y. Zhang, Y. P. Loh, J. Q. Tng, M. C. Lim, Z. Cao, A. Raju, E. L. Aiden, S. Li, L.
949 Manikandan, V. Tergaonkar, G. Tucker-Kellogg, M. J. Fullwood, H3K27me3-rich genomic regions can
950 function as silencers to repress gene expression via chromatin interactions. *Nat Commun*. 12, 719 (2021).

951 39. C. Gao, L. Chen, S.-B. Tang, Q.-Y. Long, J.-L. He, N.-A. Zhang, H.-B. Shu, Z.-X. Chen, M. Wu, L.-
952 Y. Li, The epigenetic landscapes of histone modifications on HSV-1 genome in human THP-1 cells.
953 *Antivir Res*. 176, 104730 (2020).

954 40. J. Kim, C. Sun, A. D. Tran, P.-J. Chin, P. D. Ruiz, K. Wang, R. J. Gibbons, M. J. Gamble, Y. Liu, P.
955 Oberdoerffer, The macroH2A1.2 histone variant links ATRX loss to alternative telomere lengthening. *Nat*
956 *Struct Mol Biol*. 26, 213–219 (2019).

957 41. J. Arii, Host and Viral Factors Involved in Nuclear Egress of Herpes Simplex Virus 1. *Viruses*. 13,
958 754 (2021).

959 42. S. L. Bjerke, R. J. Roller, Roles for herpes simplex virus type 1 UL34 and US3 proteins in disrupting
960 the nuclear lamina during herpes simplex virus type 1 egress. *Virology*. 347, 261–276 (2006).

961 43. M. Simpson-Holley, J. Baines, R. Roller, D. M. Knipe, Herpes Simplex Virus 1 UL31 and UL34
962 Gene Products Promote the Late Maturation of Viral Replication Compartments to the Nuclear Periphery.
963 *J Virol*. 78, 5591–5600 (2004).

964 44. N. R. Leach, R. J. Roller, Significance of host cell kinases in herpes simplex virus type 1 egress and
965 lamin-associated protein disassembly from the nuclear lamina. *Virology*. 406, 127–137 (2010).

966 45. M. M. Bahnamiri, R. J. Roller, Mechanism of Nuclear Lamina Disruption and the Role of pUS3 in
967 Herpes Simplex Virus 1 Nuclear Egress. *J Virol*. 95 (2021), doi:10.1128/jvi.02432-20.

968 46. J. M. Bigalke, T. Heuser, D. Nicastro, E. E. Heldwein, Membrane deformation and scission by the
969 HSV-1 nuclear egress complex. *Nat Commun*. 5, 4131–4131 (2014).

970 47. E. B. Draganova, M. K. Thorsen, E. E. Heldwein, Nuclear Egress of Herpesviruses. *Curr Issues Mol*
971 *Biol*. 41, 125–170 (2021).

972 48. K. L. Lynch, M. R. Dillon, M. Bat-Erdene, H. C. Lewis, R. J. Kaai, E. A. Arnold, D. C. Avgousti, A
973 viral histone-like protein exploits antagonism between linker histones and HMGB proteins to obstruct the
974 cell cycle. *Curr Biol* (2021), doi:10.1016/j.cub.2021.09.050.

975 49. S. M. Brown, D. A. Ritchie, J. H. Subak-Sharpe, Genetic Studies with Herpes Simplex Virus Type 1.
976 The Isolation of Temperature-sensitive Mutants, their Arrangement into Complementation Groups and
977 Recombination Analysis Leading to a Linkage Map. *J Gen Virol*. 18, 329–346 (1973).

978 50. C. E. Lilley, C. T. Carson, A. R. Muotri, F. H. Gage, M. D. Weitzman, DNA repair proteins affect the
979 lifecycle of herpes simplex virus 1. *P Natl Acad Sci Usa*. 102, 5844–5849 (2005).

980 51. E. M. Hatch, A. Kulukian, A. J. Holland, D. W. Cleveland, T. Stearns, Cep152 interacts with Plk4 and
981 is required for centriole duplication. *J Cell Biol*. 191, 721–729 (2010).

982 52. G. Li, C. C. Nguyen, B. J. Ryckman, W. J. Britt, J. P. Kamil, A viral regulator of glycoprotein
983 complexes contributes to human cytomegalovirus cell tropism. *Proc National Acad Sci*. 112, 4471–4476
984 (2015).

985 53. S. J. Child, A. L. Greninger, A. P. Geballe, Rapid adaptation to human protein kinase R by a unique
986 genomic rearrangement in rhesus cytomegalovirus. *Plos Pathog*. 17, e1009088 (2021).

987 54. M. Aubert, N. M. Boyle, D. Stone, L. Stensland, M.-L. Huang, A. S. Magaret, R. Galetto, D. J.
988 Rawlings, A. M. Scharenberg, K. R. Jerome, In vitro Inactivation of Latent HSV by Targeted
989 Mutagenesis Using an HSV-specific Homing Endonuclease. *Mol Ther Nucleic Acids*. 3, e146 (2014).

990 55. H. S. Kaya-Okur, S. J. Wu, C. A. Codomo, E. S. Pledger, T. D. Bryson, J. G. Henikoff, K. Ahmad, S.
991 Henikoff, CUT&Tag for efficient epigenomic profiling of small samples and single cells. *Nat Commun*.
992 10, 1930 (2019).

993 56. M. Lawrence, W. Huber, H. Pagès, P. Aboyoun, M. Carlson, R. Gentleman, M. T. Morgan, V. J.
994 Carey, Software for Computing and Annotating Genomic Ranges. *Plos Comput Biol*. 9, e1003118 (2013).

995 57. R. C. Team, R: A Language and Environment for Statistical Computing. *R Foundation for Statistical*
996 *Computing* (2019) (available at https://www.R-project.org).

997 58. A. Dobin, C. A. Davis, F. Schlesinger, J. Drenkow, C. Zaleski, S. Jha, P. Batut, M. Chaisson, T. R.
998 Gingeras, STAR: ultrafast universal RNA-seq aligner. *Bioinformatics*. 29, 15–21 (2013).

999 59. L. Wang, S. Wang, W. Li, RSeQC: quality control of RNA-seq experiments. *Bioinformatics*. 28,
1000 2184–2185 (2012).

1001 60. Y. Liao, G. K. Smyth, W. Shi, featureCounts: an efficient general purpose program for assigning
1002 sequence reads to genomic features. *Bioinformatics*. 30, 923–930 (2014).

1003 61. M. D. Robinson, D. J. McCarthy, G. K. Smyth, edgeR: a Bioconductor package for differential
1004 expression analysis of digital gene expression data. *Bioinformatics*. 26, 139–140 (2010).

1005 62. A. R. Quinlan, I. M. Hall, BEDTools: a flexible suite of utilities for comparing genomic features.
1006 *Bioinformatics*. 26, 841–842 (2010).

1007 63. T. J. Atherton, D. J. Kerbyson, Size invariant circle detection. *Image Vision Comput*. 17, 795–803
1008 (1999).

1009